

ACE-Brain-0: Spatial Intelligence as a Shared Scaffold for Universal Embodiments

Ziyang Gong^{1,2*}, Zehang Luo^{1*}, Anke Tang^{1*}, Zhe Liu^{1,5*}, Shi Fu³, Zhi Hou^{1†,‡}, Ganlin Yang⁶, Weiyun Wang⁷, Xiaofeng Wang¹, Jianbo Liu¹, Gen Luo⁸, Haolan Kang⁵, Shuang Luo³, Yue Zhou⁹, Yong Luo¹⁰, Li Shen¹¹, Xiaosong Jia⁷, Yao Mu², Xue Yang^{2‡}, Chunxiao Liu¹, Junchi Yan², Hengshuang Zhao⁵, Dacheng Tao^{3‡}, Xiaogang Wang^{1‡}

¹ACE Robotics, ²Shanghai Jiao Tong University, ³Nanyang Technological University,

⁴The Chinese University of Hong Kong, ⁵The University of Hong Kong,

⁶University of Science and Technology of China, ⁷Fudan University, ⁸Xiamen University,

⁹East China Normal University, ¹⁰Wuhan University, ¹¹Sun Yat-sen University

*Equal contribution, †Project Leader, ‡Corresponding author

Abstract

Universal embodied intelligence demands robust generalization across heterogeneous embodiments, such as autonomous driving, robotics, and unmanned aerial vehicles (UAVs). However, existing embodied brain in training a unified model over diverse embodiments frequently triggers long-tail data, gradient interference, and catastrophic forgetting, making it notoriously difficult to balance universal generalization with domain-specific proficiency. In this report, we introduce **ACE-Brain-0**, a generalist foundation brain that unifies spatial reasoning, autonomous driving, and embodied manipulation within a single multimodal large language model (MLLM). Our key insight is that spatial intelligence serves as a universal scaffold across diverse physical embodiments: although vehicles, robots, and UAVs differ drastically in morphology, they share a common need for modeling 3D mental space, making spatial cognition a natural, domain-agnostic foundation for cross-embodiment transfer. Building on this insight, we propose the **Scaffold-Specialize-Reconcile** (SSR) paradigm, which first establishes a shared spatial foundation, then cultivates domain-specialized experts, and finally harmonizes them through **data-free model merging**. Furthermore, we adopt Group Relative Policy Optimization (GRPO) to strengthen the model’s comprehensive capability. Extensive experiments demonstrate that ACE-Brain-0 achieves competitive and even state-of-the-art performance across 24 spatial and embodiment-related benchmarks.

Date: March 4, 2026

Project Page: <https://ace-brain-team.github.io/ACE-Brain-0/>

Code: <https://github.com/ACE-BRAIN-Team/ACE-Brain-0>

Hugging Face: <https://huggingface.co/ACE-Brain/ACE-Brain-0-8B>

Contents

1	Introduction	3
2	ACE-Brain-0 Architecture	5
2.1	Task Formulation	5
2.2	Multimodal Architecture	6
2.3	Multimodal Autoregressive Objective	7
3	Training Strategy	7
3.1	Stage 1: Spatial Scaffold Training	7
3.2	Stage 2: Supervised Specialized Expert Fine-Tuning	7
3.3	Stage 3: Across-Embodiment Reconcile Model Merging	7
3.4	Stage 4: Supervised Fine-Tuning on Embodied Data	8
3.5	Stage 5: Reinforcement Learning with GRPO	8
4	Experiments	9
4.1	Spatial Intelligence	9
4.2	Autonomous Driving Intelligence	9
4.3	Low-Altitude Intelligence	10
4.4	Embodied Egocentric Intelligence	11
5	Ablation Study	12
5.1	Spatial Intelligence as a Shared Scaffold	12
5.2	Importance of Data-free Model Merging (Reconcile)	12
5.3	Effectiveness of Scaffold-Specialize-Reconcile Training Paradigm	14
6	Training Datasets	15
6.1	General Datasets	15
6.2	Spatial Intelligence Datasets	15
6.3	Autonomous Driving Datasets	16
6.4	Low-Altitude Datasets	17
6.5	Embodied & Egocentric Datasets	18
7	Evaluation Details	18
7.1	Evaluation with LMMs-Eval	19
7.2	Evaluation with Official Code	19
8	Conclusions and Perspectives	20
A	Appendix	30
A.1	Mathematical Foundations of the Spatial Scaffold Mechanism	30
A.2	Gradient Interference and the Necessity of Isolation Training	31
A.3	Spatial Scaffold as a Universal Bridge: A Transfer Bound	33
A.4	Visualization on Spatial Benchmarks	36
A.5	Visualization on AD Benchmarks	36
A.6	Visualization on UAV Benchmarks	37
A.7	Visualization on Embodied Benchmarks	37

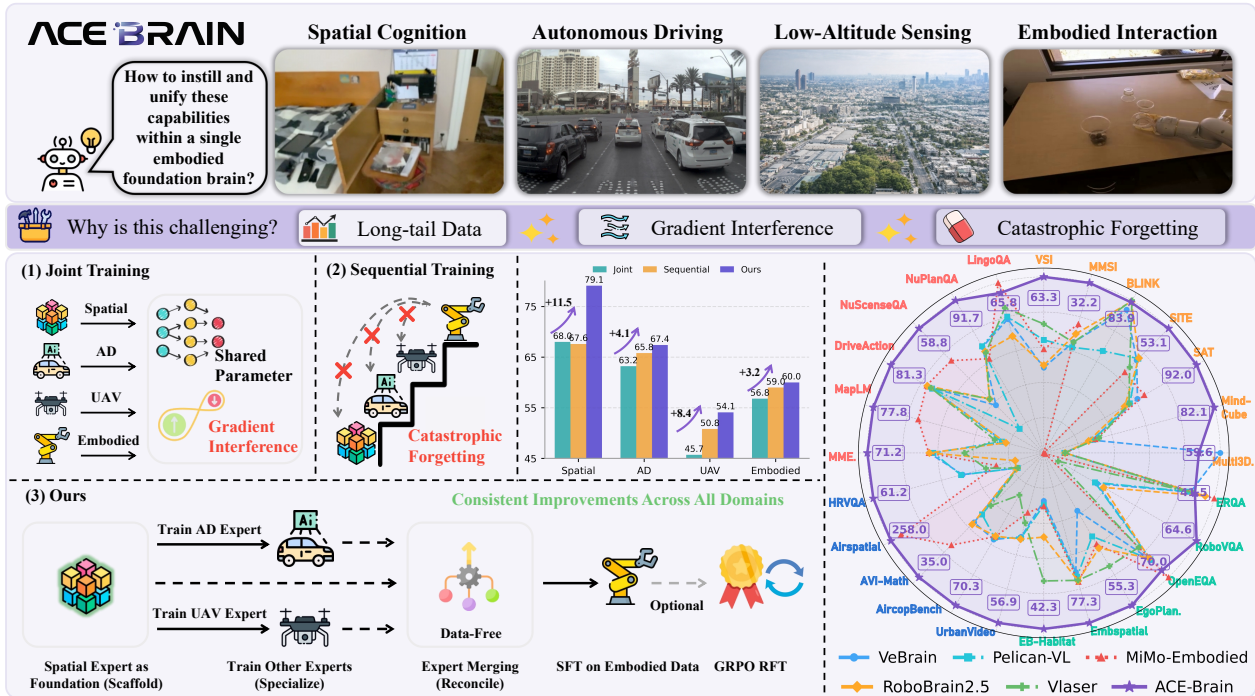


Figure 1 Cross-Embodiment Learning Paradigm of ACE-Brain-0 and Performance Comparison with other Embodied Brains. ACE-Brain-0 unifies tasks from four domains, Spatial Cognition, Autonomous Driving, Low-Altitude Sensing, and Embodied Manipulation. We hope to answer: “How can we instill and unify these capabilities within a single embodied foundation brain?” Conventional joint training mixes multi-domain data with shared parameters, which often causes gradient interference across tasks; sequential training accumulates skills via stage-wise fine-tuning, but tends to overwrite previously learned capabilities and leads to catastrophic forgetting. In contrast, we propose our Scaffold-Specialize-Reconcile paradigm: We first construct a Spatial Expert as a universal foundational model, then train the AD and UAV experts separately to acquire domain-specific skills while enabling coarse-grained spatial reasoning, and subsequently combine their expertise into a unified model via data-free expert merging. We further perform Embodied SFT, optionally followed by GRPO-based RFT for reward-guided post-training alignment. This pipeline delivers consistent and stable improvements across all four domains. The radar chart on the right further compares ACE-Brain-0 against representative embodied brains across multiple benchmarks, showing stronger overall performance on a broader set of tasks, and validating the unified cross-embodiment capability of ACE-Brain-0.

1 Introduction

Building embodied agents capable of perceiving, reasoning, and acting in the physical world demands intelligence far beyond isolated tasks or single modalities. In practice, such physical intelligence requires integrating temporal-spatial understanding, decision-making, planning, and so on. These capabilities are indispensable across diverse domains, including autonomous driving [1–6], low-altitude sensing [7–17], and embodied interaction [18–25]. Recent advances in multimodal large language models (MLLMs) [26–36] have demonstrated impressive generalization across vision-language tasks, inspiring a surge of research into spatial understanding [37–47] and embodied foundation models [48–56]. Despite rapid advances in MLLMs, developing a *generalist embodied foundation brain* that unifies these heterogeneous capabilities within a single model remains a central challenge.

Existing approaches toward this goal fall short in two complementary ways. Joint training over mixed embodiment data frequently suffers from long-tail distributions, severe task interference, and diluted domain specialization, as conflicting gradients from heterogeneous domains compromise each other’s optimization landscape. Alternatively, sequential domain-specific fine-tuning can sharpen performance on a target domain but inevitably incurs catastrophic forgetting of previously acquired abilities. These failure modes reveal that

the core bottleneck is not merely data diversity or model capacity, but rather the absence of a principled mechanism to **organize, integrate, and preserve** cross-embodiment physical knowledge.

In this work, we identify a key structural insight that opens a path forward: **spatial intelligence serves as a shared scaffold across diverse embodiments**. Although autonomous driving, robotic interaction, and low-altitude sensing differ drastically in morphology and action space, they share a fundamental reliance on 3D spatial understanding, perceiving object layouts, thinking about geometric relations, and predicting spatial consequences of actions. This common denominator makes spatial modeling a natural, domain-agnostic foundation that can scaffold and catalyze learning across otherwise disparate physical domains.

Furthermore, this spatial foundation naturally anchors a **coarse-to-fine cognitive progression: from spatial perception, to high-level planning, and ultimately to fine-grained action**. Specifically, autonomous driving and low-altitude sensing primarily demand spatial-aware planning capabilities, functioning as Vision-and-Language Navigation (VLN) tasks that focus on trajectory planning or behavior decision-making. Conversely, embodied interaction requires fine-grained execution, aligning with Vision-Language-Action (VLA) paradigms that govern low-level kinematic control and precise object manipulation.

Building on this insight, we introduce **ACE-Brain-0**, a generalist foundation brain that unifies spatial cognition, autonomous driving, low-altitude sensing [57–66], and embodied interaction within a single MLLM. To effectively harness spatial intelligence as a universal scaffold while preserving domain-specific proficiency, we propose the **Scaffold-Specialize-Reconcile (SSR)** training paradigm. As shown in Fig. 1, SSR operates in three phases: 1) **Scaffold**: Establish a shared spatial foundation that encodes domain-agnostic 3D understanding as a universal structural prior. 2) **Specialize**: Cultivate domain-specialized experts that build upon the spatial scaffold to acquire embodiment-specific capabilities. 3) **Reconcile**: Harmonize heterogeneous experts into a unified model through **data-free model merging**, avoiding both gradient interference from joint training and catastrophic forgetting from sequential training. The SSR-trained model thus serves as a new foundation for subsequent capability expansion. On top of this, we further integrate embodied interaction data to enable finer-grained embodied knowledge acquisition. Finally, a Reinforcement Fine-Tuning (RFT) strategy can be optionally employed to amplify targeted competencies.

Extensive evaluation across **24** embodiment-related benchmarks demonstrates that ACE-Brain-0 achieves competitive and even state-of-the-art performance across all targeted domains. In visual spatial intelligence, it attains top results on SAT [67] (92.0%) and Mindcube-Tiny [68] (82.1%), significantly outperforming both open-source and closed-source models. In autonomous driving, ACE-Brain-0 reaches 71.2% on MME-RealWorld [69] and 91.7% on NuPlanQA [70], while setting new records on low-altitude benchmarks, including UrbanVideo-Bench [11] (56.9%) and AircopBench [8] (70.3%). Crucially, ablation studies confirm that the SSR paradigm consistently avoids the catastrophic forgetting observed in sequential training and surpasses the limited gains of joint training, validating our core hypothesis that principled expert synthesis is fundamental to organizing heterogeneous physical knowledge.

In summary, our main contributions are as follows: 1) We identify **spatial intelligence as a shared scaffold** for cross-embodiment transfer, empirically demonstrating that a shared spatial foundation substantially boosts learning across diverse physical domains; 2) We propose the **Scaffold-Specialize-Reconcile** training paradigm, which decouples shared spatial structure from domain-specific specialization and reconciles heterogeneous experts via data-free model merging, effectively resolving the stability-plasticity dilemma. 3) We build **ACE-Brain-0**, a generalist foundation brain that achieves competitive and even state-of-the-art performance across **24** benchmarks spanning spatial cognition, autonomous driving, low-altitude sensing, and embodied interaction (shown in Fig. 2), which provides a principled blueprint for generalist embodied AI.

The remainder of this report is organized as follows. Section 2 presents the multimodal auto-regressive architecture of ACE-Brain-0. The proposed Scaffold-Specialize-Reconcile training strategy, covering five stages from base knowledge acquisition to GRPO reinforcement learning, is detailed in Section 3. Section 4 reports extensive experimental results and Section 5 presents the ablation analyses that validate our core findings on spatial scaffolding and expert reconciliation. Section 6 describes the multi-domain training corpus, spanning general multimodal instructions, embodied manipulation, autonomous driving, and low-altitude aerial datasets. Section 7 introduces the evaluation benchmarks. Finally, Section 8 concludes with perspectives on future

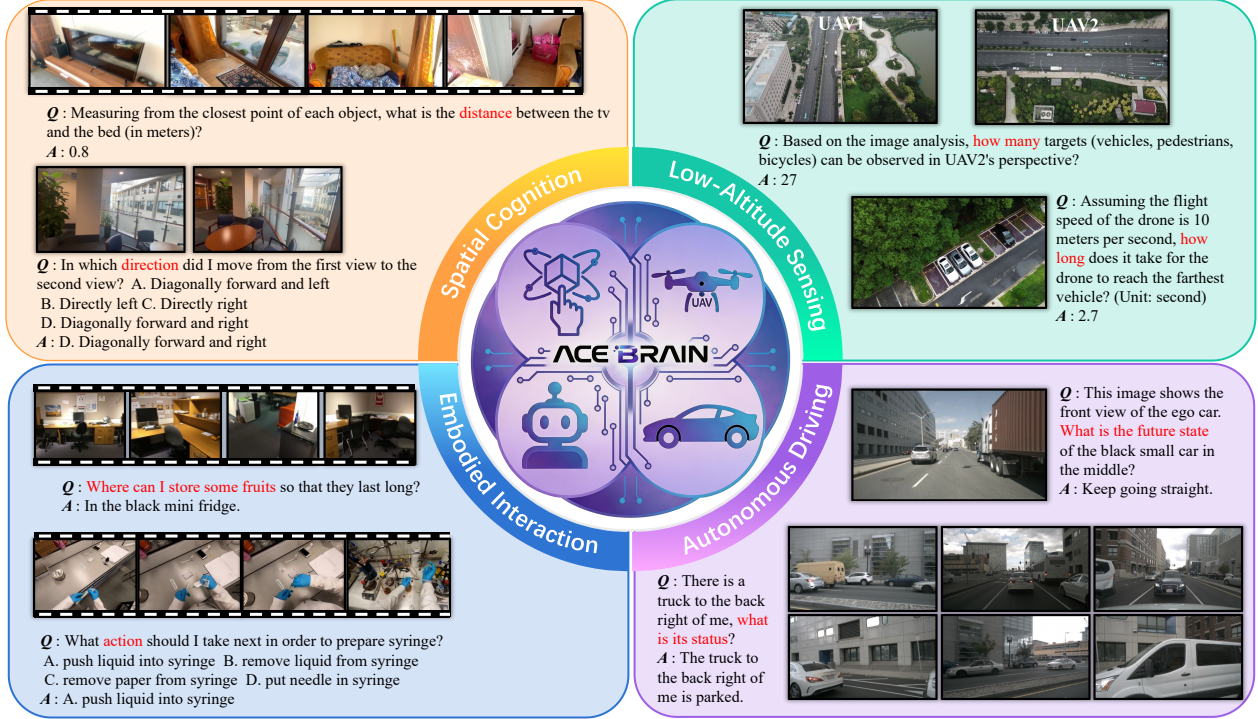


Figure 2 Overview of ACE-Brain-0 Capabilities. ACE-Brain-0 is a spatial-centric foundation brain that supports Spatial Intelligence, Embodied Manipulation, Low-Altitude Sensing, and Autonomous Driving. Specifically, ACE-Brain-0 is evaluated on 7 benchmarks for Spatial Cognition, 6 benchmarks for Autonomous Driving, 5 benchmarks for Low-Altitude Sensing, and 6 benchmarks for Embodied Interaction. ACE-Brain-0’s ability to integrate perception, decision, and planning across diverse real-world embodied scenarios, highlighting its generalization capability as a universal embodied intelligence model.

generalist embodied agents.

2 ACE-Brain-0 Architecture

2.1 Task Formulation

We consider a cross-domain embodiment learning setting, where a single MLLM is trained to perform tasks arising from distinct embodied agent forms. We denote the set of domains as $\mathcal{M} = \{m_1, m_2, \dots, m_K\}$. Specifically, we consider the following domains in this work:

$$\mathcal{M} = \{m_{\text{general}}, m_{\text{embodied}}, m_{\text{spatial}}, m_{\text{driving}}, m_{\text{aerial}}\}, \quad (1)$$

encompassing general, spatial, autonomous driving, and low-altitude domains. Each $m_k \in \mathcal{M}$ induces a specific task distribution \mathcal{D}_{m_k} over training samples (o, c, y) , where (1) $o \in \mathcal{O}_{m_k}$ denotes multimodal observations (images or video sequences); (2) $c \in \mathcal{C}$ denotes task conditioning, including natural language instructions, queries, or high-level goals; and (3) $y \in \mathcal{Y}_{m_k}$ denotes the target output, which may be textual responses, reasoning traces, spatial descriptions, action sequences, or planning trajectories depending on the task. Despite substantial heterogeneity across observation spaces \mathcal{O}_{m_k} and output formats \mathcal{Y}_{m_k} , we model all tasks using a unified conditional autoregressive formulation:

$$p_{\theta}(y \mid o, c), \quad (2)$$

where θ denotes the parameters of a single shared MLLM. This design choice enforces a common representational backbone and thinking substrate across all embodiments, enabling knowledge transfer and compositional generalization.

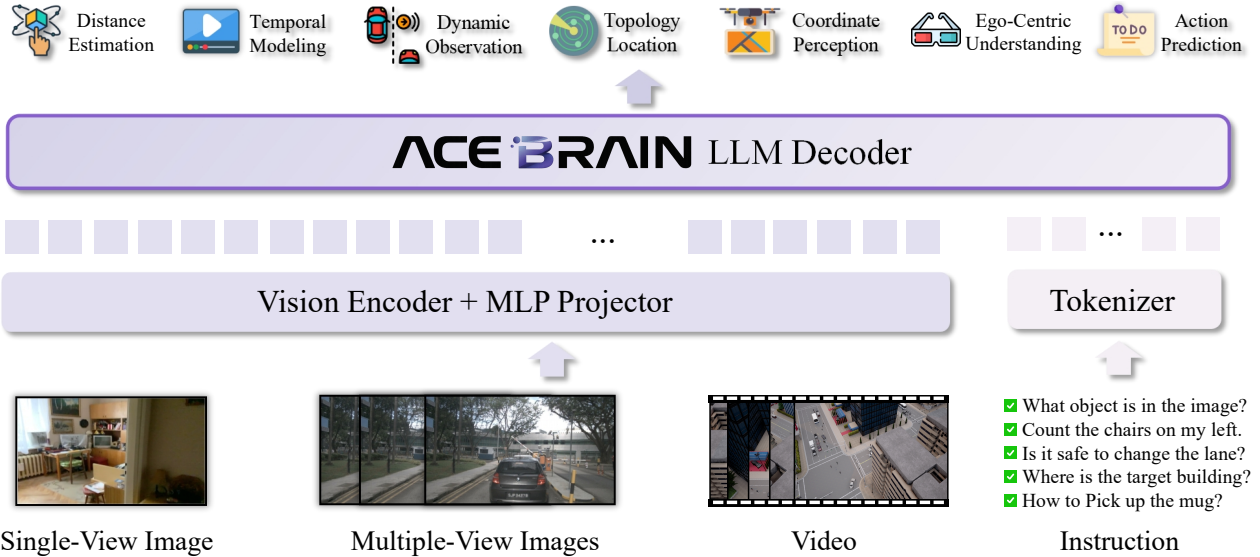


Figure 3 ACE-Brain-0’s unified multimodal architecture and cross-domain capability coverage. ACE-Brain-0 supports inputs including single-view images, multi-view images, and videos; the instruction examples illustrate that the model can perform Q&A-style tasks across domains (General/Spatial/Driving/Aerial/Embodied). The top row summarizes ACE-Brain-0’s core capability spectrum for cross-embodiment scenarios, such as Spatial Perception and Temporal Modeling, enabling unified representation and compositional generalization across domains.

2.2 Multimodal Architecture

As shown in Figure 3, ACE-Brain-0 adopts a multimodal autoregressive architecture, following recent designs of MLLM [71]. The model consists of three core components: a Vision Encoder paired with an MLP Projector, a Tokenizer, and the ACE-Brain-0 LLM Decoder.

The model accepts diverse visual inputs, including single-view images, multiple-view images, and video, together with natural language instructions. This flexibility enables ACE-Brain-0 to handle a broad spectrum of embodied tasks, from static scene understanding to temporal reasoning over video sequences. All visual inputs are processed by a Vision Encoder, which extracts rich visual features regardless of the input modality or domain. The extracted features are then projected into the language model’s embedding space through an MLP Projector. Notably, the resulting visual tokens are conceptually organized by domain into five categories—*General*, *Spatial*, *Driving*, *Aerial*, and *Embodied*. Natural language instructions and queries are converted into text tokens by the Tokenizer. These text tokens serve as task conditioning, specifying the desired output format, domain context, or action space for each query.

The domain-organized visual tokens and text tokens are concatenated into a unified sequence and fed into the ACE-Brain-0 LLM Decoder, which autoregressively generates output tokens. This unified decoder enables the model to jointly attend to visual and textual information, supporting a wide range of output capabilities, such as *Spatial Perception*, *Temporal Modeling*, *Trajectory Prediction*, *Safety Control*, *Aerial Location*, *Multi-UAV Cooperation*, *Embodied Interaction*, *Task Planning*, and so on.

Formally, given visual observations $o \in \mathbb{R}^{T \times H \times W \times 3}$ (e.g., single-view images with $T=1$, multiple-view images, or video frames) and textual conditioning c (e.g., instructions or queries), the model predicts the next-token distribution as follows:

$$p = \mathcal{F}_{\text{dec}}\left(t_N \mid \mathcal{F}_{\text{proj}}(\mathcal{F}_{\text{enc}}(o; \theta_{\text{enc}}); \theta_{\text{proj}}), \mathcal{F}_{\text{tok}}(c), t_{0:N-1}; \theta_{\text{dec}}\right), \quad (3)$$

where $\mathcal{F}_{\text{enc}}(\cdot; \theta_{\text{enc}})$ denotes the Vision Encoder, $\mathcal{F}_{\text{proj}}(\cdot; \theta_{\text{proj}})$ denotes the MLP Projector, $\mathcal{F}_{\text{tok}}(\cdot)$ denotes the Tokenizer, and $\mathcal{F}_{\text{dec}}(\cdot; \theta_{\text{dec}})$ denotes the LLM Decoder. The output $p \in \mathbb{R}^m$ represents the probability distribution over a vocabulary of size m , and t_i denotes the i -th generated token.

2.3 Multimodal Autoregressive Objective

Given a training sample (o, c, y) where y denotes the target output (e.g., textual answers, thinking traces, or action sequences), the MLLM processes the observation o and conditioning text c into a unified token sequence $\mathbf{s} = (s_1, \dots, s_L)$, where the first tokens correspond to encoded visual features and input text, followed by the target output tokens from y . We adopt the standard left-to-right autoregressive objective:

$$\mathcal{L}_{\text{full}}(\theta) = - \sum_{i=1}^L w_i \log p_{\theta}(s_i | s_{<i}), \quad (4)$$

where w_i denotes the loss weight of token s_i , and $s_{<i} = (s_1, \dots, s_{i-1})$ denotes the preceding context. Following common practice in MLLM training, loss computation is restricted to text tokens only, while visual tokens serve as conditioning context and are not directly predicted. This yields the supervised objective:

$$\mathcal{L}_{\text{Text}}(\theta) = - \sum_{i=1, s_i \in \text{Text}}^L w_i \log p_{\theta}(s_i | s_{<i}). \quad (5)$$

Regarding the choice of token weights w_i , naive token averaging or sample averaging may introduce biases toward longer or shorter responses. To mitigate this issue, we adopt square averaging, which balances gradient contributions across samples with different sequence lengths.

3 Training Strategy

In this section, we describe the training methodology of **ACE-Brain-0**. Our training strategy follows a staged paradigm, which progressively builds shared multimodal representations, morphology-specific expertise, and finally a unified policy capable of generalizing across embodied domains.

3.1 Stage 1: Spatial Scaffold Training

In Stage 1, our primary objective is to train an expert model with spatial cognition capabilities. This stage consists of two main steps: first, we train a base model θ_{base} based on Qwen3-VL θ using general data [72] to perform early activation through instruction tuning; second, we train a spatial expert model using large-scale spatial data from θ_{base} . The spatial expert θ_{spatial} will serve as the central node to provide a shared universal scaffold for the following experts' training.

3.2 Stage 2: Supervised Specialized Expert Fine-Tuning

Starting from the spatial expert model $\{\theta_{\text{spatial}}, \theta_{\text{uav}}, \theta_{\text{ad}}\}$, where each expert is initialized independently on data sampled from its corresponding distribution. This isolation prevents gradient interference between domains with conflicting optimization objectives.

Specifically, we have: (1) θ_{spatial} : Expert model specialized in spatial cognition modeling, trained on spatial intelligence datasets. (2) θ_{uav} : Expert model trained on θ_{spatial} and specialized in low-altitude sensing, location, and navigation for Unmanned Aerial Vehicles (UAV). (3) θ_{ad} : Expert model trained on θ_{spatial} and specialized in autonomous driving perception, planning, and control, trained on driving-specific datasets.

3.3 Stage 3: Across-Embodiment Reconcile Model Merging

At this stage, we merge these expert models into a single unified model through a cross-embodiment merging procedure in a data-free manner. The goal of this stage is to synthesize complementary capabilities learned by each expert while mitigating interference. The first systematic attempt to introduce adaptivity into multi-task model merging was made by AdaMerging [73], which learns task-specific merging coefficients and demonstrates clear advantages over fixed-weight baselines. Building on this line of work, Shen et al. [74] propose what is arguably the most effective and efficient weight-ensembling mixture-of-experts framework to date, providing both theoretical justification and strong empirical evidence on large-scale multi-task benchmarks. We adopt

the optimization-based Merging algorithm [75, 76], which approximates the linear subspace of fine-tuning data for each expert by the task vector τ , which is computed as the difference between the expert model parameters and the base model parameters. The merging process begins with an initialization of the merged model as the average of all expert models $\theta_{\text{merge}}^{(0)} = \frac{1}{K} \sum_{i=1}^K \theta_i$. Then, we iteratively optimize the merged model parameters to minimize the task interference across all experts as follows:

$$\theta_{\text{merge},l}^* = \arg \min_{\theta_{\text{merge},l}} \sum_{i=1}^K \mathbb{E}_{x_{i,l} \sim \mathcal{D}_{m_i,l}} \|\theta_{i,l} x_{i,l} - \theta_{\text{merge},l} x_{i,l}\|_2^2 \quad (6)$$

$$= \theta_l + \arg \min_{\tau_{\text{merge},l}} \sum_{i=1}^K \mathbb{E}_{x_{i,l} \sim \mathcal{D}_{m_i,l}} \|\tau_{i,l} x_{i,l} - \tau_{\text{merge},l} x_{i,l}\|_2^2, \quad (7)$$

where θ denotes the parameters of the base model, l denotes the l -th layer of the model, and $\mathcal{D}_{m_i,l}$ denotes the approximated data distribution for the i -th morphology expert at layer l . By analyzing the update dynamics of the task vector, we derive the following upper bound on task interference:

$$\mathbb{E}_{x_{i,l} \sim \mathcal{D}_{m_i,l}} \|(\theta_{i,l} - \tau_{\text{merge},l}) x_{i,l}\|_2^2 \leq \omega_{i,l}^1 \cdot \|(\theta_{i,l} - \tau_{\text{merge},l})(\tau_{i,l})^\top\|_F^2 + \omega_{i,l}^2 \cdot \|\theta_{i,l} - \tau_{\text{merge},l}\|_F^2, \quad (8)$$

where $\omega_{i,l}^1$ and $\omega_{i,l}^2$ are constants, and the proof is provided in [75]. Therefore, Eq.(7) can be rewrite as follows

$$\theta_{\text{merge},l}^* \approx \theta_{\text{pre},l} + \arg \min_{\tau_{\text{merge},l}} \sum_{i=1}^K \frac{1}{\|\tau_{i,l}\|_F^2} \|(\tau_{\text{merge},l} - \tau_{i,l}) \tau_{i,l}^\top\|_F^2, \quad (9)$$

The optimization of the merged task vector τ_{merge} is performed using the Adam optimizer with a learning rate of 1e-5, weight decay set to 0, and 1,000 iterations, implemented via the FusionBench framework [77]. The merging methods also can be changed to any other data-free methods, and here we also explored alternative merging techniques, including SVD-based Task Singular Vector Merging (TSVM) [78] and vanilla parameter averaging (also known as ModelSoups) [79, 80]. We provide detailed comparisons between merging-based approaches and data mixing strategies in Section 4.

3.4 Stage 4: Supervised Fine-Tuning on Embodied Data

After cross-embodiment merging, the unified model θ_{merged} undergoes embodied-enhanced supervised fine-tuning to obtain θ_{embodied} . This stage focuses on further strengthening models' embodied capability. The training data comprises large-scale embodied and ego-centric multimodal data pairs that emphasize consistent embodied interaction, task planning, and action prediction. This refinement step ensures that the model can reliably interpret embodied instructions and generate appropriate responses while maintaining the spatial and cross-embodied capabilities acquired through merging.

3.5 Stage 5: Reinforcement Learning with GRPO

Finally, the θ_{embodied} is further refined through preference-based reinforcement learning to obtain θ_{GRPO} with 100k mixed data from spatial, ad, uav, and embodied corpus. We adopt Group Relative Policy Optimization (GRPO) [81], which optimizes the model using relative rewards computed from multiple sampled responses to the same query. Specifically, for each question q , GRPO samples a group of G outputs $\{o_1, o_2, \dots, o_G\}$ from the old policy $\pi_{\theta_{\text{old}}}$ and optimizes the policy by maximizing:

$$\mathcal{J}_{\text{GRPO}}(\theta) = \mathbb{E}_{\{o_i\}_{i=1}^G \stackrel{q \sim P(Q)}{\sim} \pi_{\theta_{\text{old}}}(\cdot|q)} \frac{1}{G} \sum_{i=1}^G \frac{1}{|o_i|} \sum_{t=1}^{|o_i|} \left[\min \left(\frac{\pi_{\theta}(o_{i,t}|q, o_{i,<t})}{\pi_{\theta_{\text{old}}}(o_{i,t}|q, o_{i,<t})} \hat{A}_{i,t}, \text{clip} \left(\frac{\pi_{\theta}(o_{i,t}|q, o_{i,<t})}{\pi_{\theta_{\text{old}}}(o_{i,t}|q, o_{i,<t})}, 1-\varepsilon, 1+\varepsilon \right) \hat{A}_{i,t} \right) \right], \quad (10)$$

where ε is the clipping hyper-parameter for stabilizing training and $\hat{A}_{i,t}$ is the group-relative advantage. Note that, refer to [36], we omit the KL divergence penalty term against a reference policy in our implementation, as we empirically find that the clipped surrogate objective alone provides sufficient regularization for stable

Table 1 Details of Scaffold-Specialize-Reconcile training strategy of ACE-Brain-0.

	Stage-1	Stage-2	Stage-3	Stage-4	Stage-5
Target Objective	Scaffold SFT	Specialize SFT	Expert Reconcile	Embodied SFT	RTF
Data Domain	Spatial	AD,UAV	- (Data-Free)	Embodied	Mixed
Base Model	θ_{base}	θ_{spatial}	$\theta, \theta_{\text{spatial}}, \theta_{\text{ad}}, \theta_{\text{uav}}$	θ_{merge}	θ_{embodied}
Trainable Part	MLP, LLM	MLP, LLM	MLP, LLM	MLP, LLM	MLP, LLM
Per-device Batch Size	8	8	-	8	8 / 256
Gradient Accumulation	4	4	0	4	8
Epoch/Step	1	1	1,000 steps	1	1
Optimizer	AdamW	AdamW	Adam	AdamW	AdamW
LR	5×10^{-6}	5×10^{-6}	1×10^{-5}	5×10^{-6}	1×10^{-6}
Deepspeed	Zero2	Zero2	-	Zero2	-
Weight Decay	0.0	0.0	0.0	0.0	0.01
Warmup Ratio	0.03	0.03	-	0.03	0.0
LR Schedule	cosine	cosine	-	cosine	constant
Min Pixels	50176	50176	-	50176	50176
Max Pixels	50176	50176	-	50176	50176
Video Min Pixels	200,704	200,704	-	200,704	-
Video Max Pixels	802,816	802,816	-	802,816	-
Model Max Length	16384	16384	-	16384	8192

training in our embodied setting. The advantage $\hat{A}_{i,t}$ is computed from group-normalized rewards without requiring a learned value function. A reward model scores each output o_i , yielding rewards $\{r_1, r_2, \dots, r_G\}$. Under outcome supervision, the rewards are normalized within the group and assigned uniformly to all tokens:

$$\hat{A}_{i,t} = \tilde{r}_i = \frac{r_i - \text{mean}(\mathbf{r})}{\text{std}(\mathbf{r})}, \quad (11)$$

where $\mathbf{r} = \{r_1, \dots, r_G\}$. By leveraging GRPO, the model learns to optimize for decision quality under uncertainty and the ability to handle multi-step task planning required in complex spatial and embodied scenarios.

4 Experiments

4.1 Spatial Intelligence

As shown in Table 2, we evaluate ACE-Brain-0 on seven visual spatial benchmarks (*i.e.*, VSI [82], MMSI [83], BLINK [84], SITE [85], SAT [67], MindCube [68], and Multi3DRef [86]), collectively covering spatial relationship comprehension, 3D referring grounding, temporal memorization, viewpoint transformation, and mental spatial modeling. ACE-Brain-0-8B achieves consistently strong performance across all benchmarks, matching or surpassing both closed-source MLLMs and state-of-the-art embodied brains. In spatial relationship and distance understanding, ACE-Brain-0 reaches 83.9% on BLINK, outperforming Gemini2.5-Pro (81.8%), and 63.3% on VSI, surpassing both Gemini2.5-Pro (47.8%) and the strongest embodied brain Vlaser (60.3%). For viewpoint transformation and mental modeling, it obtains 92.0% on SAT, largely exceeding Gemini2.5-Pro (79.3%) and MiMo-Embodied-7B (78.7%), while on MindCube it achieves 82.1%, far ahead of Gemini2.5-Pro (57.6%), GPT-4o (46.1%), and Vlaser-8B (34.6%). In scene understanding and 3D grounding, ACE-Brain-0 reaches 53.1% on SITE, exceeding InternVL3.5-8B (50.1%) and RoboBrain2.5-8B (52.6%) while remaining competitive with Gemini2.5-Pro (57.0%); on Multi3DRef, our result of 59.6% surpasses most open-source MLLMs and embodied brains, though VeBrain-7B (67.8%) retains the lead.

4.2 Autonomous Driving Intelligence

As shown in Table 3, we evaluate ACE-Brain-0 on six autonomous driving benchmarks (MME-RealWorld [69], MAPLM [90], DriveAction [91], NuscenesQA [92], NuPlanQA [70], and LingoQA [93]), collectively cover-

Table 2 Performance Comparison on Spatial Benchmarks. Bold numbers indicate the best results, underlined numbers indicate the second-best results, and results marked with * are obtained using our evaluation framework.

Model	VSI	MMSI	BLINK	SITE	SAT	Mindcube	Multi3DRef
<i>Closed-source MLLMs</i>							
GPT-4o [87]	43.6	<u>30.3</u>	77.9	37.8	66.7	46.1	8.1
Gemini-2.5-Pro [26]	47.8	38.0	81.8	57.0	79.3	57.6	–
Claude-4-Sonnet [88]	<u>47.0</u>	–	<u>78.1</u>	–	<u>75.3</u>	36.6	–
Qwen-VL-Max [71]	41.8	–	–	–	56.7	–	–
<i>Open-source general-purpose MLLMs</i>							
MiMo-VL-7B [89]	36.4	–	–	37.6	59.3	–	8.1
Qwen2.5-VL-7B-Inst. [30]	32.3	26.8	82.5*	31.4	52.0	<u>36.0</u>	21.1*
InternVL3-8B [35]	42.1	25.7	82.9*	41.1	72.7*	41.5	8.1*
InternVL3.5-8B [36]	56.3	<u>30.2*</u>	<u>84.1*</u>	50.1*	59.3	35.1*	8.1*
Qwen3-VL-2B-Inst. [71]	53.9	29.7*	74.9	35.6	<u>67.3*</u>	34.5	–
Qwen3-VL-8B-Inst. [71]	59.4	31.0*	85.2	<u>45.8</u>	66.0*	29.4	54.6*
<i>Embodied Brain MLLMs</i>							
RoboBrain2.0-7B [49]	36.1	27.9	81.4*	49.2*	75.3	31.2*	8.1*
RoboBrain2.5-8B [50]	41.0*	29.3*	<u>84.3*</u>	<u>52.6*</u>	63.3*	28.1*	8.1*
VeBrain-7B [53]	39.9	27.3*	79.7	51.4*	73.3*	30.1*	67.8*
Pelican-VL-7B [54]	52.8	26.0*	56.8	52.3*	67.3*	31.0*	7.9*
MiMo-Embodied-7B [51]	48.5	<u>31.7*</u>	0.0*	44.8	<u>78.7</u>	32.3*	8.1*
Vlaser-8B [52]	<u>60.3</u>	27.2	84.9*	47.5*	66.7*	<u>34.6*</u>	8.1*
ACE-Brain-0-8B	63.3	32.2	83.9	53.1	92.0	82.1	<u>59.6</u>

ing multi-view traffic perception, planning-aware language modeling, action recognition, ego-centric scene understanding, and language-grounded driving semantics.

ACE-Brain-0-8B achieves consistently strong results across all benchmarks, outperforming closed-source MLLMs, open-source general MLLMs, and state-of-the-art embodied brains in most cases. In object understanding under the driving scenarios, ACE-Brain-0 reaches 71.2% on MME-RealWorld, surpassing Gemini2.5-Pro (67.0%), Qwen3-VL-8B-Inst (63.3%), and MiMo-Embodied-7B (60.3%), and obtains 77.8% on MAPLM, substantially exceeding the strongest embodied brain baseline MiMo-Embodied-7B (74.5%). In action understanding and scene QA, it achieves 81.3% on DriveAction, outperforming Gemini2.5-Pro (73.5%) and MiMo-Embodied-7B (81.0%), while on NuscenesQA it reaches 58.8%, largely exceeding GPT-4o (34.3%) and MiMo-Embodied-7B (56.7%). In physical kinematics comprehension and decision making, ACE-Brain-0 attains 91.7% on NuPlanQA, where models need integrate surround-view inputs with kinematic cues to produce driving justifications, outperforming Pelican-VL-7B (83.4%) and RoboBrain2.0-7B (82.8%); on LingoQA, it achieves 65.8%, exceeding Gemini2.5-Pro (64.1%) and Vlaser-8B (59.6%), demonstrating the ability to generate interpretable, causally grounded behavior descriptions.

Overall, these results suggest that ACE-Brain-0 does not merely memorize driving templates but learns an ego-centric, multi-view consistent driving representation that bridges perception, kinematics, and language into decision-relevant reasoning, supporting reliable next-step prediction and interpretable interaction within complex traffic environments.

4.3 Low-Altitude Intelligence

As shown in Table 4, we evaluate ACE-Brain-0 on five low-altitude UAV benchmarks (*i.e.*, UrbanVideoBench [11], AircopBench [8], Avi-Math [59], Airspatial-VQA [10], and HRVQA [94]), collectively covering aerial location, navigation, bird’s-eye traffic-scene reasoning, and geometry-aware visual computation under drastic viewpoint changes.

Table 3 Performance Comparison on Autonomous Driving Benchmarks.

Model	MME-RealWorld	MAPLM	DriveAction	NuscenesQA	NuPlanQA	LingoQA
<i>Closed-source MLLMs</i>						
GPT-4o [87]	58.0	26.6	72.5	34.3	81.5	56.0
Gemini2.5-pro [26]	67.0	<u>26.1</u>	73.5	<u>16.1</u>	–	64.1
Claude-4-Sonnet [88]	–	–	–	–	–	–
Qwen-VL-Max [71]	<u>61.7</u>	24.8	<u>72.6</u>	6.7	–	<u>58.8</u>
<i>Open-source general-purpose MLLMs</i>						
MiMo-VL-7B [89]	54.1	31.0	<u>78.9</u>	33.9	–	54.8
Qwen2.5-VL-7B-Inst. [30]	<u>58.6</u>	24.8	73.4	<u>25.8</u>	41.8	<u>55.6</u>
InternVL3-8B [35]	52.1*	<u>31.0*</u>	77.6*	26.6*	82.7*	50.8*
InternVL3.5-8B [36]	49.2	14.2	78.1	17.2	83.9*	46.7
Qwen3-VL-2B-Inst. [71]	–	20.5*	77.1*	–	66.7*	34.8*
Qwen3-VL-8B-Inst. [71]	63.3*	31.5*	79.0*	22.8*	82.2*	57.0*
<i>Embodied Brain MLLMs</i>						
RoboBrain2.0-7B [49]	59.6*	31.7*	80.9*	32.3*	82.8*	39.2*
RoboBrain2.5-8B [50]	60.0*	22.5*	80.5*	33.2*	79.3*	48.0*
VeBrain-7B [53]	60.1*	22.9*	78.3*	29.3*	82.9*	55.0*
Pelican-VL-7B [54]	57.9*	24.4*	77.2*	14.8	83.4*	56.0*
MiMo-Embodied-7B [51]	<u>60.3</u>	<u>74.5</u>	<u>81.0</u>	<u>56.7</u>	73.7*	69.9
Vlaser-8B [52]	41.6*	29.1*	78.1*	33.1*	78.3*	59.6*
ACE-Brain-0-8B	71.2	77.8	81.3	58.8	91.7	<u>65.8</u>

ACE-Brain-0-8B delivers consistently strong results across all benchmarks, with clear advantages in the most decision-relevant UAV settings. In aerial location and safety-critical scene reasoning, ACE-Brain-0 achieves 56.9% on UrbanVideo-Bench, outperforming Qwen-VL-Max (45.5%), GPT-4o (43.6%), and RoboBrain2.5-8B (37.5%), and reaches 70.3% on AircopBench, which requires resolving topology-aware spatial relations such as crosswalk occupancy and lane-aware ordering, largely surpassing GPT-4o (51.8%) and InternVL3-8B (52.2%). In quantitative aerial reasoning and high-resolution understanding, ACE-Brain-0 obtains 35.0% on Avi-Math, outperforming Qwen2.5-VL-7B-Inst. (27.9%) and MiMo-Embodied-7B (33.7%), demonstrating competence in region-conditioned counting, altitude estimation, and physics-based computation (Fig. 31); on HRVQA, it achieves 61.2%, significantly exceeding InternVL3-8B (37.6%) and Pelican-VL-7B (38.6%).

4.4 Embodied Egocentric Intelligence

As shown in Table 5, we evaluate ACE-Brain-0 on six embodied benchmarks, including ERQA [95], RoboVQA [96], OpenEQA [97], EmbSpatial-Bench [98], EgoPlan-Bench2 [99], and EmbodiedBench(EB)-Habitat [100], collectively covering embodied interaction, egocentric planning, and next-step prediction under temporal observations.

ACE-Brain-0-8B achieves consistently strong results across all benchmarks, outperforming or matching both general-purpose MLLMs and state-of-the-art embodied brains. In embodied interaction and egocentric scene understanding, ACE-Brain-0 reaches 64.6% on RoboVQA, surpassing GPT-4o (34.5%), Gemini2.5-Pro (33.9%), Qwen2.5-VL-7B-Inst. (57.2%), and MiMo-Embodied-7B (32.8%), and obtains 70.0% on OpenEQA, exceeding Qwen3-VL-8B-Inst. (67.1%), VeBrain-7B (63.8%), and RoboBrain2.5-8B (62.6%), while remaining competitive with MiMo-Embodied-7B (74.1%). In sequential decision-making and temporal reasoning, ACE-Brain-0 achieves 55.3% on EgoPlan-Bench2, delivering the best overall result and outperforming Qwen3-VL-8B-Inst. (53.5%), Vlaser-8B (53.4%), and RoboBrain2.5-8B (44.9%); on EB-Habitat, it obtains 41.7%, exceeding Vlaser-8B (40.0%) and RoboBrain2.0-7B (29.3%), showing solid generalization to longer-horizon embodied environments. In embodied spatial comprehension, ACE-Brain-0 reaches 77.3% on EmbSpatial-Bench, largely

Table 4 Performance Comparison on Low-Altitude Benchmarks.

Model	UrbanVideo-Bench	AircopBench	Avi-Math	Airspatial-VQA	HRVQA
<i>Closed-source MLLMs</i>					
GPT-4o [87]	<u>43.6</u>	51.8	33.5	192.4	36.9
Gemini2.5-pro [26]	–	49.1	–	–	–
Claude-4-Sonnet [88]	–	<u>50.7</u>	–	–	–
Qwen-VL-Max [71]	45.5	50.5	–	–	–
<i>Open-source general-purpose MLLMs</i>					
MiMo-VL-7B [89]	–	48.6*	–	–	27.3*
Qwen2.5-VL-7B-Inst. [30]	<u>34.6*</u>	47.3	27.9	–	27.1*
InternVL3-8B [35]	30.8*	52.2	<u>26.8</u>	337.0	37.6*
InternVL3.5-8B [36]	<u>34.6*</u>	23.6*	23.3*	1507.0	14.6*
Qwen3-VL-2B-Inst. [71]	30.5*	38.3*	11.6*	–	<u>37.5*</u>
Qwen3-VL-8B-Inst. [71]	39.2*	48.7*	25.6*	<u>1254.4*</u>	37.4*
<i>Embodied Brain MLLMs</i>					
RoboBrain2.0-7B [49]	30.0*	47.2*	22.1*	764.4*	19.2*
RoboBrain2.5-8B [50]	<u>37.5*</u>	49.9*	26.1*	1509.3*	13.4*
VeBrain-7B [53]	36.5*	<u>51.9*</u>	25.4*	1583.4*	37.9*
Pelican-VL-7B [54]	37.1*	50.8*	22.5*	1586.6*	<u>38.6*</u>
MiMo-Embodied-7B [51]	26.0*	50.2*	<u>33.7*</u>	<u>289.4*</u>	22.2*
Vlaser-8B [52]	30.4*	25.3*	19.3*	1597.7*	27.0*
ACE-Brain-0-8B	56.9	70.3	35.0	258.0	61.2

exceeding RoboBrain2.0-7B (76.3%) and InternVL3-8B (73.9%), while staying close to the strongest results of Gemini2.5-Pro (78.7%) and Qwen3-VL-8B-Inst. (78.5%).

5 Ablation Study

5.1 Spatial Intelligence as a Shared Scaffold

It is widely believed that strong visual spatial intelligence benefits physical world comprehension, yet its actual impact is rarely quantified, especially across embodiments. To explicitly measure how spatial knowledge transfers, we compare multiple training and adaptation routes on three domains: autonomous driving (AD), low-altitude aerial intelligence (UAV), and embodied intelligence (Embodied). As summarized in Table 6, domain experts trained directly from the base model (Qwen3-VL-8B-Instruct) already yield clear gains over the base model on AD and UAV benchmarks, confirming that domain-specific data alone improves in-domain performance. However, we carefully find that there is 1.9% performance degradation on the Embodied benchmark compared with the base model. Compared with AD and UAV benchmarks, we argue that the Embodied benchmark needs more fine-grained capability in action understanding (fine-grained manipulation vs. coarse-grained planning), making it difficult to transfer directly from the general domain of the base model to the embodied domain. Crucially, when initializing these experts from a spatial-centric pretrained checkpoint, our framework yields substantial and consistent improvements: +19.3% in AD, +16.5% in UAV, and +5.4% in Embodied over the base model. These results provide compelling empirical evidence that spatial knowledge functions as a transferable structural scaffold that catalyzes learning across universe embodiments, rather than an isolated capability confined to spatial understanding benchmarks.

5.2 Importance of Data-free Model Merging (Reconcile)

A fundamental challenge in developing generalist physical intelligence lies in the effective integration of heterogeneous domain knowledge. In this work, we investigate the efficient composition of domain-specific

Table 5 Performance Comparison on Embodied Benchmarks.

Model	ERQA	RoboVQA	OpenEQA	EmbSpatial	Ego-Plan2	EB-Habitat
<i>Closed-source MLLMs</i>						
GPT-4o [87]	<u>47.0</u>	3.3	56.4	<u>71.9</u>	41.8	59.0
Gemini2.5-pro [26]	48.3	–	–	78.7	<u>42.9</u>	–
Claude-4-Sonnet [88]	–	–	–	64.3	41.3	–
Qwen-VL-Max [71]	–	–	–	–	44.7	<u>45.3</u>
<i>Open-source general-purpose MLLMs</i>						
MiMo-VL-7B [89]	37.8	35.3	–	–	34.1	–
Qwen2.5-VL-7B-Inst. [30]	38.8	57.2*	59.9*	–	39.7	14.3
InternVL3-8B [35]	35.3	29.8*	68.3*	<u>73.9*</u>	37.9*	24.3
InternVL3.5-8B [36]	<u>41.5</u>	28.6	64.9*	70.3	<u>42.9</u>	32.0*
Qwen3-VL-2B-Inst. [71]	28.3	18.2*	56.4*	69.2*	33.6*	–
Qwen3-VL-8B-Inst. [71]	45.8	<u>47.0*</u>	<u>67.1*</u>	78.5*	53.5*	<u>27.7*</u>
<i>Embodied Brain MLLMs</i>						
RoboBrain2.0-7B [49]	42.5*	6.6*	60.0*	<u>76.3*</u>	33.2	29.3
RoboBrain2.5-8B [50]	<u>44.3*</u>	18.7*	62.6*	75.6*	44.9*	26.3*
VeBrain-7B [53]	40.3*	24.7*	63.8*	70.5*	27.3	15.0*
Pelican-VL-7B [54]	39.8	23.6*	63.3*	73.2*	39.4*	16.3*
MiMo-Embodied-7B [51]	46.8	<u>32.8*</u>	74.1*	76.2*	43.0	16.7*
Vlaser-8B [52]	41.0	7.9*	56.3*	75.3*	<u>53.4</u>	<u>40.0</u>
ACE-Brain-0-8B	41.5	64.6	<u>70.0</u>	77.3	55.3	42.3

Table 6 Spatial knowledge consistently improves expert performance. We compare different pretraining routes for adapting to three domains (AD, UAV, and Embodied). The average score of AD is computed over NuscenQA, NuPlanQA, and LingoQA benchmarks; the average score of UAV is computed over UrbanVideoBench, AircopBench, and Avi-Math; the average score of Embodied is computed over RoboVQA and EgoPlan. **Bold** indicates the best score, and improvements (Δ) are reported over Qwen3-VL-8B-Instruct.

Initialization / Route	AD		UAV		Embodied	
	Avg.	Δ	Avg.	Δ	Avg.	Δ
Qwen3-VL-8B-Instruct (θ)	47.0	–	37.8	–	<u>52.7</u>	–
AD Experts ($\theta \rightarrow \theta_A$)	<u>58.1</u>	<u>+11.1</u>	–	–	–	–
UAV Experts ($\theta \rightarrow \theta_U$)	–	–	<u>48.8</u>	<u>+11.0</u>	–	–
Embodied Experts ($\theta \rightarrow \theta_E$)	–	–	–	–	50.8	-1.9
Spatial \rightarrow AD Expert ($\theta_S \rightarrow \theta_A$)	72.6	+25.6	–	–	–	–
Spatial \rightarrow UAV Expert ($\theta_S \rightarrow \theta_U$)	–	–	54.3	+16.5	–	–
Spatial \rightarrow Embodied Expert ($\theta_S \rightarrow \theta_E$)	–	–	–	–	58.1	+5.4

experts into a unified model through data-free parameter merging. Specifically, we evaluate three merging strategies, which include the naive weight averaging, TSVM, and WUDI on three domains: Spatial, AD, and UAV. Notably, all methods operate without requiring additional training data during composition, with results summarized in Tab. 7. Across all domains, parameter merging consistently outperforms the base model, demonstrating its ability to effectively synthesize domain expertise. While simple averaging yields noticeable improvements, TSVM further enhances performance, suggesting that domain-specific knowledge is largely complementary and can be reconciled at the parameter level. Among the evaluated strategies, WUDI achieves the most robust results. It not only leads in all domains but also surpasses the strongest individual specialists (e.g., 76.7% in Spatial and 68.1% in AD). This highlights a super-additive composition

Table 7 Optimized Merging effectively combines each domain. The average score of Spatial is computed over VSI, SAT, and MindCube benchmarks.

Training / Synthesis Strategy	Spatial		AD		UAV	
	Avg.	Δ	Avg.	Δ	Avg.	Δ
Qwen3-VL-8B-Instruct (θ)	51.6	-	47.0	-	37.8	-
Spatial (θ_S)	72.5	+20.9	-	-	-	-
Spatial \rightarrow AD ($\theta_S \rightarrow \theta_A$)	-	-	72.6	+25.6	-	-
Spatial \rightarrow UAV ($\theta_S \rightarrow \theta_U$)	-	-	-	-	54.3	+16.5
Merging weights of $\theta_0, \theta_{0 \rightarrow S}, \theta_{S \rightarrow A}, \theta_{S \rightarrow U}$						
AVG Merging (θ_{avg})	71.6	+20.0	66.6	+19.6	48.0	+10.2
TSVM Merging (θ_{tsvm})	<u>74.8</u>	<u>+23.2</u>	<u>72.8</u>	<u>+25.8</u>	51.4	+13.6
WUDI Merging (θ_{wudi})	76.7	+25.1	72.9	+25.9	<u>52.6</u>	<u>+14.8</u>

Table 8 Training paradigm comparison. We compare four paradigms: **Joint** trains on mixed {Spatial, AD, UAV, Embodied} data; **Sequential** performs stage-wise adaptation Spatial \rightarrow AD \rightarrow UAV \rightarrow Embodied; **SR** follows Spatial \rightarrow Merging \rightarrow Embodied.

Training Paradigm	Spatial		AD		UAV		Embodied	
	Avg.	Δ	Avg.	Δ	Avg.	Δ	Avg.	Δ
Spatial (θ_S)	72.5	-	-	-	-	-	-	-
Spatial \rightarrow AD Expert ($\theta_S \rightarrow \theta_A$)	-	-	72.6	-	-	-	-	-
Spatial \rightarrow UAV Expert ($\theta_S \rightarrow \theta_U$)	-	-	-	-	54.3	-	-	-
Spatial \rightarrow Embodied Expert ($\theta_S \rightarrow \theta_E$)	-	-	-	-	-	-	58.1	-
Joint Training	68.0	-4.5	65.3	-7.3	45.7	-8.6	56.8	-1.3
Sequential Training	67.6	-4.9	70.1	-2.5	50.8	-3.5	59.0	+0.9
SSR Training	78.5	+6.0	72.0	-0.6	50.9	-3.2	59.7	+1.6
SSR Training w/ GRPO	79.1	+6.6	72.1	-0.5	<u>54.1</u>	<u>-0.2</u>	60.0	+1.9

effect rather than mere parameter ensembling, positioning optimized merging as a pivotal mechanism for integrating complementary expertise into unified models.

5.3 Effectiveness of Scaffold-Specialize-Reconcile Training Paradigm

Building on the preceding empirical analyses, we introduce the Scaffold-Specialize-Reconcile (SSR) training paradigm for cross-embodied physical world comprehension. Under matched total training budgets, we compare SSR against two prevalent alternatives: joint training on mixed data and sequential multi-stage adaptation without merging.

As shown in Table 8, joint training, directly mixing spatial, AD, and UAV data prior to embodied finetuning, yields limited and inconsistent gains across domains. Sequential training without synthesis improves the final target domain (Embodied) but incurs catastrophic forgetting on previously learned capabilities, corroborating the degradation patterns observed in earlier sections. In contrast, SSR achieves consistently strong performance across all domains. The paradigm proceeds in four stages: establishing a domain-agnostic spatial scaffold, training domain-specialized experts, reconciling these experts through optimized merging, and finally performing embodied alignment. This structured decomposition effectively integrates heterogeneous physical knowledge while preserving domain-specific strengths. Notably, SSR improves Embodied performance without sacrificing Spatial, AD, or UAV capabilities, achieving superior generalization-specialization trade-offs compared to baselines.

These findings underscore the importance of expert synthesis in embodied learning. While model merging has been extensively studied in language and vision domains, its application to physical intelligence remains underexplored. Our results indicate that synthesis constitutes more than a parameter-level heuristic—it serves as a fundamental mechanism for organizing and reusing heterogeneous physical knowledge. Collectively, the empirical evidence supports the SSR paradigm as a principled training strategy for multi-robot and cross-embodied foundation models.

Building upon the preceding empirical analyses, we propose the Scaffold-Specialize-Reconcile (SSR) training paradigm for cross embodiments. To verify the effectiveness of the SSR training paradigm, we provide two prevalent strategies, including the joint training strategy on mixed datasets and the sequential training strategy by using multi-stage adaptation without merging. As shown in Table 8, the joint training strategy by mixing Spatial, AD, and UAV data before embodied fine-tuning yields only marginal gains. Although the sequential training strategy enhances performance in the final target domain (*e.g.*, Embodied), it suffers from catastrophic forgetting of previously acquired capabilities, leading to worse performance in earlier domains (*e.g.*, AD and UAV). In contrast, SSR delivers robust performance across all domains. This structured decomposition effectively integrates heterogeneous physical knowledge while preserving domain-specific proficiencies. Notably, SSR bolsters Embodied performance without compromising Spatial, AD, or UAV capabilities, achieving a superior generalization-specialization trade-off compared to existing training paradigms.

6 Training Datasets

A central challenge in training a generalist embodied brain lies in harmonizing different embodiment data. These datasets diverge not only in visual appearance but also in their implicit spatial assumptions, temporal organization, and task-level planning demands. To this end, we construct a training corpus shown in Fig. 4. It spans general multimodal instruction, spatial intelligence, autonomous driving, and low-altitude aerial datasets. Next, we will briefly introduce them.

6.1 General Datasets

We begin by establishing a shared multimodal foundation that anchors visual perception, language understanding, and instruction following. Here, we adopt the Cambrain-737K [72] visual instruction-tuning dataset. It samples built upon the LLaVA-665K [101] foundation, augmented with additional OCR-rich and chart-understanding corpora, to enhance document perception capabilities. This composition ensures balanced coverage across general VQA, text-rich image comprehension, and structured reasoning tasks, providing a robust corpus for aligning visual representation with language instruction.

6.2 Spatial Intelligence Datasets

Agent interaction with the world implicitly relies on consistent spatial-temporal representations. To support this requirement, we include spatial intelligence datasets that focus on object relations, distance measurement, and spatial layouts in both static and dynamic video inputs.

VSI-590K [82] is a large-scale visual spatial intelligence dataset comprising 590K QA pairs. The dataset spans diverse question types, including size, direction, distance, count, and temporal order across viewpoints and modalities (images and videos).

SAT [67] is a generated spatial dataset built on photo-realistic ProcTHOR-10K [102] environments, containing 175K QA pairs across 22K indoor scenes without manual 3D annotation.

VICA-322K [103] is a large-scale video-based spatial dataset built on real-world indoor videos with high-quality 3D annotations. It combines metadata-supervised spatial tasks (*e.g.*, object count, size, distance, and room scale) that require holistic interpretation of spatial layouts and object relationships over videos.

GPT4Scene [104] is a large-scale indoor 3D scene understanding dataset with 165K annotations paired with processed videos for VLM fine-tuning. It integrates sampled video frames, reconstructed 3D point clouds, BEV images, and spatio-temporal object markers to maintain consistent object identities across views and

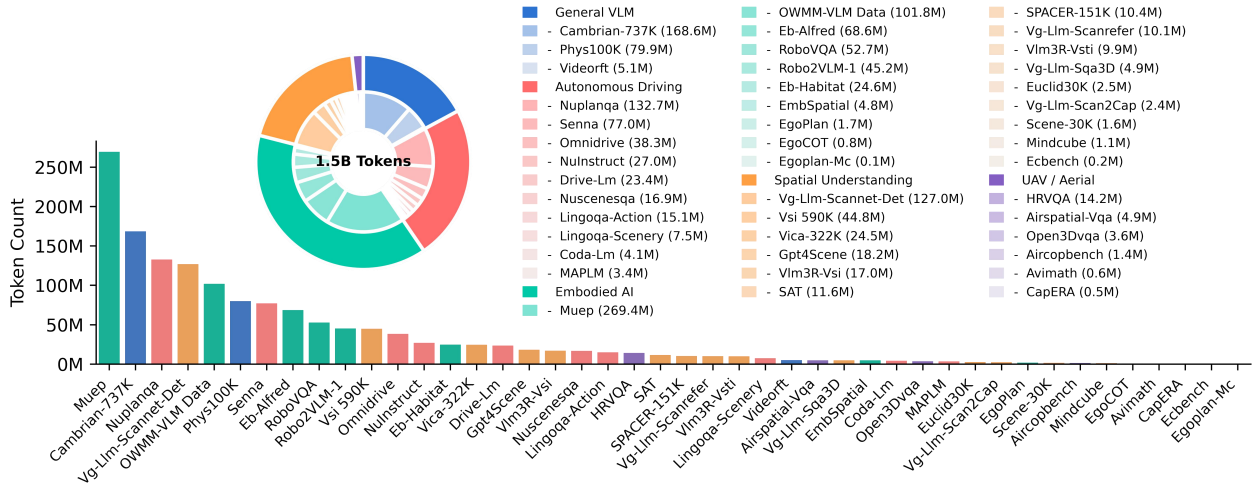


Figure 4 Domain distribution and Token count. This nested pie chart illustrates the proportion of tokens contributed by each domain. The distribution exhibits a long-tailed characteristic, where UAV data constitutes a relatively small proportion of the corpus.

time. Built via 3D reconstruction and instance segmentation pipelines, it supports vision-only 3D spatial tasks such as 3D QA, dense captioning, and visual grounding.

Scene-30K [105] is a synthetic 30K CoT dataset for enhancing 3D VLM reasoning. It covers a wide range of 3D scene understanding tasks, including captioning, QA, grounding, dialogue, reasoning, and planning. Constructed from existing 3D-VL datasets and generated using a Gemini-2.5-Pro-based pipeline, it provides multi-step reasoning annotations filtered for structural correctness and semantic consistency.

VLM-3R [106] consists of two datasets, VSI and VSTI, targeting 3D spatial understanding from static scenes and monocular videos, respectively. VLM-3R-VSI contains over 200K QA pairs. Similar to VSI [82], it is also built from ScanNet [107], ScanNet++ [108], and ARKitScenes [109]. VLM-3R-VSTI comprises 138.6K video QA pairs for spatio-temporal understanding, spanning camera dynamics, camera-object interactions, and object relative position. It focuses on estimating camera motion, movement direction, and evolving relative distances without relying on explicit 3D reconstructions or depth sensors.

EmbSpatial-Bench [98] is an instruction-tuning dataset for improving embodied spatial understanding in MLLMs. Constructed from Matterport3D [110], it contains 25K samples covering spatial relation recognition and object localization as an auxiliary grounding task.

MindCube [68] is a rigorously annotated benchmark with 10k SFT data where all questions require reasoning over unobservable space. Built from multi-view image groups with controlled camera trajectories, it emphasizes cross-view consistency, occlusion handling, and viewpoint-dependent relations, serving as a challenging testbed for evaluating internal spatial mental model construction.

SpaceR-151K [111] is a video spatial reasoning dataset comprising 151K QA pairs, designed to enhance spatial intelligence in MLLMs.

6.3 Autonomous Driving Datasets

Autonomous driving datasets provide supervision for perception, prediction, and planning in complex traffic scenarios. These datasets capture diverse driving conditions, weather variations, and interaction dynamics essential for training robust driving intelligence.

MAPLM [112] is a large-scale vision-language benchmark specifically engineered for autonomous driving, focusing on map and traffic scene understanding. It moves beyond simple object detection by requiring models to reason about lane-level topology, road geometry, and complex traffic rules. By providing a diverse set of

real-world driving scenarios, MAPLM serves as a critical testbed for evaluating the potential of foundation models in enhancing the decision-making and spatial understanding capabilities of autonomous vehicles.

DriveAction [113] is a pioneering dataset designed to explore human-like driving decisions within Vision-Language-Action (VLA) models. It shifts the focus from pure perception to the closed-loop integration of multimodal understanding and actionable decision-making.

Nuscenes-QA [114] is a large-scale multimodal VQA dataset specifically designed for autonomous driving scenarios. By leveraging the comprehensive sensor data from the nuScenes dataset, it provides over 460K VQA pairs that require models to perform complex spatial and temporal understanding across 360-degree multi-view camera inputs.

NuPlanQA [70] extends the scope of driving scene understanding by providing a large-scale VQA dataset based on the nuPlan dataset. It focuses on multi-view visual understanding and the interpretation of complex driving maneuvers, offering a comprehensive platform to test the limits of MLLMs in understanding real-world, planning-centric autonomous driving scenarios.

LingoQA [115] introduces a specialized Visual Question Answering benchmark for autonomous driving that emphasizes the model’s ability to explain driving scenes. A key contribution of this work is the introduction of *Lingo-Judge*, a learned evaluation metric that aligns more closely with human judgment than traditional linguistic metrics. LingoQA challenges models to provide temporally consistent and safety-critical explanations for various driving behaviors and environmental conditions.

6.4 Low-Altitude Datasets

Low-altitude aerial perception presents unique challenges, including viewpoint variation, scale estimation from altitude, and interpretation of terrain features from oblique perspectives.

HRVQA [94] presents a large-scale dataset with over 100k qa pairs. It can be used to evaluate the capabilities of VQA models in performing scene understanding and geospatial understanding for high-resolution aerial images.

AirSpatial-VQA [10] is a pioneering monocular 3D spatial perception dataset centered on vehicles captured by UAV aerial imagery. Based on photogrammetric principles and the ground plane assumption, this dataset establishes a benchmark for evaluating the 3D spatial understanding capabilities of MLLMs in drone-based scenarios. The benchmark tasks encompass vehicle 3D coordinates, 3D dimensions (length, width, height), and depth estimation. It aims to advance the monocular spatial perception of low-altitude intelligent systems, enabling zero-shot vehicle model recognition from aerial views.

Open3DVQA [116] is a benchmark for evaluating MLLMs’ ability to reason about complex spatial relationships from an aerial perspective. It contains 89k QA pairs across 7 spatial understanding tasks, including multiple-choice, true/false, and short-answer formats, and supports both visual and point cloud data.

AirCopBench [117] evaluates MLLMs’ ability to answer questions using multi-UAV collaborative visual data under perception-degraded conditions, covering perception, understanding, and decision-making. It comprises over 2.9k multi-view images and 14.6k VQA pairs across four core tasks consisting of scene understanding, object Understanding, perception assessment, and collaborative decision.

AVIMath [59] introduces a multimodal mathematical understanding benchmark based on UAV aerial imagery. This dataset spans six mathematical disciplines-geometry, arithmetic, algebra, statistics, logic, and counting-covering 20 fine-grained topics and comprising 3,773 high-quality problems. The images are sourced from 11 distinct 4K scenes, captured with three pitch angles (45°, 60°, 90°) and three flight altitudes (low, medium, high), thereby closely simulating real-world UAV acquisition conditions.

CapERA [118] evaluates whether MLLMs can generate natural-language descriptions for aerial videos captured by UAVs. The dataset comprises 2,864 videos and 14,320 diverse captions, each video paired with five human-aligned textual descriptions generated through manual annotation and automatic augmentation. CapERA emphasizes comprehensive scene understanding, including events, objects, actions, locations, and temporal dynamics.

6.5 Embodied & Egocentric Datasets

To support embodied interaction and egocentric perception, we incorporate datasets that capture first-person visual experiences and action-oriented understanding.

MuEP [119] is a comprehensive multimodal dataset specifically tailored for embodied planning with foundation models. Covering 108 varied household scenes and nearly 15,000 expert demonstration episodes, it facilitates the evaluation of multimodal and multi-turn interactions. By incorporating fine-grained metrics, MuEP assesses the agent’s performance throughout task execution, effectively bridging the gap between high-level reasoning and low-level control in complex environments.

OWMM-VLM Data [120] is a synthesized dataset designed for open-world mobile manipulation. Generated using the Habitat simulator and PDDL-based task sequences, it provides comprehensive supervision for global scene understanding, robot state tracking, and multimodal action generation. This dataset provides supervision for reasoning over multi-view observations and generating action affordances grounded in both the robot’s state and the environment geometry.

Eb-Alfred [121] and **Eb-Habitat** [122] serve as the core simulation datasets for long-horizon household task planning. To significantly enhance the model’s ability to comprehend complex instructions, decompose tasks, and execute actions based on environmental feedback, we adopted a rigorous re-annotation pipeline. Specifically, we initialized planning tasks following standard annotations (e.g., LLaRP [122]) to specify task goals and permissible actions, and then deployed a GPT-4o [87] agent to roll out the tasks in the simulator. We recorded the task instructions, action sequences, and real-time environmental observations, retaining only the trajectories that successfully accomplished the task. This LLM-driven generation provides the model with high-quality supervision containing detailed reasoning traces and successful execution paths, improving decision-making robustness in complex embodied scenarios.

RoboVQA [96] is a large-scale multimodal dataset designed for long-horizon robotic reasoning. It comprises video-text pairs covering diverse embodiments, including humans and robots. The dataset focuses on temporal grounding tasks, such as describing past events and reasoning about future affordances, thereby enhancing the model’s ability to understand the temporal dynamics of physical interactions and answer open-ended queries about the robot’s environment.

Robo2VLM [123] is a large-scale visual question answering dataset generated from in-the-wild robot manipulation trajectories. Leveraging data from various robotic platforms, it utilizes proprioceptive and kinematic states to automatically generate ground-truth QA pairs focused on spatial relations, object states, and interaction reasoning. This dataset allows the model to learn from diverse, scalable real-robot data without expensive manual annotation, bridging the gap between visual perception and physical robot states.

EgoPlan [99] is designed for egocentric embodied planning derived from real-world videos involving human-object interactions. It focuses on predicting the next feasible action based on the task progress, current visual observation, and language instruction. We also include **EgoPlan-Mc**, a multiple-choice variant, to further refine the model’s decision-making capabilities by aligning high-level task planning with intricate, real-world situations captured from a first-person perspective.

EgoCOT [124] serves as a large-scale embodied planning dataset featuring chain-of-thought (CoT) supervision. Constructed from carefully selected egocentric videos, it includes high-quality, step-by-step language instructions that are machine-generated and human-verified. This dataset is crucial for training the model to decompose complex tasks into logical intermediate reasoning steps, effectively enabling the model to solve manageable sub-tasks step by step before executing the final action.

7 Evaluation Details

We evaluate ACE-Brain-0 on 24 benchmarks, using both the off-the-shelf LMMs-Eval [125] framework and the official evaluation code provided by each benchmark.

7.1 Evaluation with LMMs-Eval

We first introduce the evaluation with LMMs-Eval. A subset of our adopted benchmarks is already supported by LMMs-Eval, and we follow their default evaluation settings. For these built-in benchmarks, we set the image resolution constraints to $maxpixels = 1024 \times 28 \times 28$ and $minpixels = 256 \times 28 \times 28$.

For benchmarks that are not natively available in LMMs-Eval, we manually integrate them into the same evaluation pipeline for consistent reporting. For these manually integrated benchmarks, we resize every evaluation image to a fixed resolution of 50,176 pixels, while keeping the number of evaluation images consistent with each benchmark’s original protocol. These benchmarks already supported in LMMs-Eval include VSI [82], MindCube-Tiny [68], Blink [84], SITE [85], MME-RealWorld [69], ERQA [95], and EmbSpatial-Bench [98].

NuScenes-QA [92] contains 83335 VQA, and each question uses six camera images with text. The model should output a short answer (a single word or an Arabic numeral). It evaluates multi-view perception and attribute/object/state recognition in road-traffic scenes. The evaluation metric is exact-match accuracy.

NuPlanQA [70] contains 1,801 multiple-choice (A-E) questions. It evaluates decision-making and traffic-element understanding in autonomous driving. The metric is accuracy.

HRVQA [94] contains 13,524 questions. Each sample uses one UAV-view image, and the model generates a free-form answer. It evaluates understanding of high-resolution visual details. The metric is exact-match and accuracy.

7.2 Evaluation with Official Code

Next, we delineate the benchmarks evaluated with their official code. **SAT** [67] contains 150 multiple-choice questions. Each question uses 1-2 images with text, and the model outputs an option letter. The metric is exact-match accuracy.

Multi3DRef [86] contains 11,120 samples. Each sample provides an indoor 3D scene with a set of objects and a natural-language referring expression; the model outputs the matching object instance IDs (one or multiple, e.g., <OBJxxx>). It evaluates multi-target referring understanding and instance-level retrieval in 3D scenes. Metric: F1@0.25, computed by matching predicted vs. ground-truth instance sets using 3D box IoU ≥ 0.25 as the threshold, then averaging F1 over all samples.

MAPLM [90] contains 6,000 multiple-choice (A-F) questions. Each question provides a set of map/traffic-related observation images, and the model outputs a single option letter. It evaluates multiple-choice reasoning and decision-making in map and driving contexts. Metrics: Accuracy, reported as the average score of question-level accuracy (QNS) and frame-level accuracy (FRM), where a frame is considered correct only if all questions from the same scene/frame are answered correctly.

DriveAction [91] contains 16,185 questions. Each question uses three images from the same driving scene, and the model outputs either True/False or an option letter (depending on the task). It evaluates action/behavior decision understanding in autonomous driving from multi-frame observations. The evaluation metric adopts exact-match accuracy.

LingoQA [93] contains 500 questions. Inputs are consecutive frames from a driving video segment, and the model generates an open-ended answer. It evaluates language understanding in driving scenes and its fusion with multi-frame visual evidence. Evaluation uses the LingoJudge discriminator to judge correctness against the reference, and reports the fraction judged correct as accuracy.

UrbanVideo-Bench [11] contains 5,355 five-choice (A-E) questions on urban egocentric videos. Each video is uniformly downsampled to up to 32 frames, and the model outputs an option letter (optionally with a brief rationale). It evaluates temporal understanding and embodied navigation reasoning in complex city scenes, covering action prediction, landmark localization, progress estimation, trajectory description, target detection, high-level planning, cognitive mapping, and counterfactual reasoning. The evaluation metric adopts accuracy.

AirCopBench [8] consists of 1,031 four-choice (A-D) questions across four subsets (Real2, Sim3, Sim5, Sim6). Inputs are multi-UAV observations, and the model outputs an option letter. It evaluates multi-view scene

and target understanding, perception quality assessment, and cooperative decision-making. The evaluation metric adopts accuracy.

AVI-Math [59] follows the official two-stage protocol: (i) free-form generation that prioritizes reasoning, and (ii) extraction into a prescribed format to reduce errors from formatting. Answers are typed via the `eva` field and normalized with type-specific rules (e.g., lowercasing strings; stripping units; rounding integers; truncating floats to one decimal).

AirSpatial-VQA [10] follows the official protocol and uses Mean Absolute Error (MAE) for five numerical spatial questions (Depth, Distance, Length, Width, Height). Lower MAE means closer estimates to the label.

RoboVQA [96] includes 1,335 trajectories, split into 1,921 open-ended questions. For each trajectory, 32 frames are uniformly sampled as input, and the model generates free-form answers. It evaluates embodied visual understanding and task reasoning, including next-step prediction/planning, affordance judgments, and state/event description. The evaluation metric adopts the average score of BLEU-1/2/3/4.

OpenEQA [97] includes 1,636 open-ended questions with 32 uniformly sampled frames per question. It evaluates indoor scene understanding under multi-frame aggregation (object recognition, attribute/state recognition, and spatial relations). Scoring uses a GPT-based 1-5 match rating averaged over all questions, also mapped to a 0-100 scale.

EgoPlan-Bench2 [99] contains 1,321 questions. We uniformly sample 16 frames from the task start to the current observation as input. It evaluates temporal task understanding for embodied interaction, next-step action planning/decision-making, and goal-directed reasoning. The evaluation metric adopts accuracy.

EmbodiedBench(EB)-Habitat [100] is a simulation benchmark built on the Habitat [126] simulator, including various vision-language conditioned decision-making tasks with 282 diverse language instructions. In these tasks, the agent needs to understand the language-described goals and use commonsense and spatial reasoning to plan with the provided skills, such as navigation, pick, and open. The evaluation metric adopts the final success rate of the task.

8 Conclusions and Perspectives

In this report, we introduce ACE-Brain-0, a generalist foundation model that unifies spatial cognition, autonomous driving, low-altitude sensing, and embodied interaction through the Scaffold-Specialize-Reconcile (SSR) paradigm. The SSR paradigm provides a blueprint for cross-embodiment learning: construct a shared spatial scaffold, cultivate domain experts in isolation, and reconcile them via parameter merging. This enables incremental capability expansion with less gradient interference and catastrophic forgetting. Evaluated on 24 benchmarks spanning four physical domains, ACE-Brain-0 achieves competitive or even state-of-the-art performance, significantly outperforming both general-purpose VLMs and domain-specific embodied brains.

Looking forward, we will advance along three axes: (1) Spatially-grounded visuomotor policies, extending ACE-Brain-0 to vision-language-action models for closed-loop control across robot embodiments; (2) Physics-aware continuous prediction, iterating beyond discrete scene understanding toward fine-grained physical world modeling; and (3) Cross-Embodiment Continual Learning, advancing the SSR paradigm toward lifelong, interference-free capability accumulation, enabling seamless integration of novel embodiments (e.g., legged locomotion, underwater vehicles).

References

- [1] Zhijian Huang, Chengjian Feng, Feng Yan, Baihui Xiao, Zequn Jie, Yujie Zhong, Xiaodan Liang, and Lin Ma. Robotron-drive: All-in-one large multimodal model for autonomous driving. In Proceedings of the IEEE/CVF International Conference on Computer Vision, pages 8011–8021, 2025.
- [2] Chonghao Sima, Katrin Renz, Kashyap Chitta, Li Chen, Hanxue Zhang, Chengen Xie, Jens Beißwenger, Ping Luo, Andreas Geiger, and Hongyang Li. Drivelm: Driving with graph visual question answering. In European conference on computer vision, pages 256–274. Springer, 2024.
- [3] Zhijian Huang, Chengjian Feng, Feng Yan, Baihui Xiao, Zequn Jie, Yujie Zhong, Xiaodan Liang, and Lin Ma. Drivemm: All-in-one large multimodal model for autonomous driving. arXiv preprint arXiv:2412.07689, 2024.
- [4] Ayesha Ishaq, Jean Lahoud, Ketan More, Omkar Thawakar, Ritesh Thawkar, Dinura Dissanayake, Noor Ahsan, Yuhao Li, Fahad Shahbaz Khan, Hisham Cholakkal, et al. Drivelmm-o1: A step-by-step reasoning dataset and large multimodal model for driving scenario understanding. arXiv preprint arXiv:2503.10621, 2025.
- [5] Zhenhua Xu, Yujia Zhang, Enze Xie, Zhen Zhao, Yong Guo, Kwan-Yee K Wong, Zhenguo Li, and Hengshuang Zhao. Drivegpt4: Interpretable end-to-end autonomous driving via large language model. IEEE Robotics and Automation Letters, 2024.
- [6] Zhe Liu, Runhui Huang, Rui Yang, Siming Yan, Zining Wang, Lu Hou, Di Lin, Xiang Bai, and Hengshuang Zhao. Drivepi: Spatial-aware 4d mllm for unified autonomous driving understanding, perception, prediction and planning. arXiv preprint arXiv:2512.12799, 2025.
- [7] Yuqi Ping, Tianhao Liang, Huahao Ding, Guangyu Lei, Junwei Wu, Xuan Zou, Kuan Shi, Rui Shao, Chiya Zhang, Weizheng Zhang, et al. Multimodal large language models-enabled uav swarm: Towards efficient and intelligent autonomous aerial systems. arXiv preprint arXiv:2506.12710, 2025.
- [8] Jirong Zha, Yuxuan Fan, Tianyu Zhang, Geng Chen, Yingfeng Chen, Chen Gao, and Xinlei Chen. Aircopbench: A benchmark for multi-drone collaborative embodied perception and reasoning. arXiv preprint arXiv:2511.11025, 2025.
- [9] Jiajin Guan, Haibo Mei, Bonan Zhang, Dan Liu, Yuanshuang Fu, and Yue Zhang. Uav-vl-r1: Generalizing vision-language models via supervised fine-tuning and multi-stage grpo for uav visual reasoning. arXiv preprint arXiv:2508.11196, 2025.
- [10] Yue Zhou, Ran Ding, Xue Yang, Xue Jiang, and Xingzhao Liu. Airspatialbot: A spatially-aware aerial agent for fine-grained vehicle attribute recognition and retrieval. IEEE Transactions on Geoscience and Remote Sensing, 2025.
- [11] Baining Zhao, Jianjie Fang, Zichao Dai, Ziyu Wang, Jirong Zha, Weichen Zhang, Chen Gao, Yue Wang, Jinqiang Cui, Xinlei Chen, et al. Urbanvideo-bench: Benchmarking vision-language models on embodied intelligence with video data in urban spaces. arXiv preprint arXiv:2503.06157, 2025.
- [12] Yue Zhou, Jue Chen, Zilun Zhang, Penghui Huang, Ran Ding, Zhentao Zou, Pengfei Gao, Yuchen Wei, Ke Li, Xue Yang, et al. Dvgbench: Implicit-to-explicit visual grounding benchmark in uav imagery with large vision-language models. ISPRS Journal of Photogrammetry and Remote Sensing, 232:831–847, 2026.
- [13] Haotian Xu, Yue Hu, Chen Gao, Zhengqiu Zhu, Yong Zhao, Yong Li, and Qianjun Yin. Geonav: Empowering mllms with explicit geospatial reasoning abilities for language-goal aerial navigation. arXiv preprint arXiv:2504.09587, 2025.
- [14] Oleg Sautenkov, Yasheerah Yaqoot, Artem Lykov, Muhammad Ahsan Mustafa, Grik Tadevosyan, Aibek Akhmetkazy, Miguel Altamirano Cabrera, Mikhail Martynov, Sausar Karaf, and Dzmitry Tsetserukou. Uav-vla: Vision-language-action system for large scale aerial mission generation. In 2025 20th ACM/IEEE International Conference on Human-Robot Interaction (HRI), pages 1588–1592. IEEE, 2025.
- [15] Yonglin Tian, Fei Lin, Yiduo Li, Tengchao Zhang, Qiyao Zhang, Xuan Fu, Jun Huang, Xingyuan Dai, Yutong Wang, Chunwei Tian, et al. Uavs meet llms: Overviews and perspectives towards agentic low-altitude mobility. Information Fusion, 122:103158, 2025.
- [16] Fei Lin, Yonglin Tian, Yunzhe Wang, Tengchao Zhang, Xinyuan Zhang, and Fei-Yue Wang. Airvista: Empowering uavs with 3d spatial reasoning abilities through a multimodal large language model agent. In 2024 IEEE 27th International Conference on Intelligent Transportation Systems (ITSC), pages 476–481. IEEE, 2024.

- [17] Fei Lin, Yonglin Tian, Tengchao Zhang, Jun Huang, Sangtian Guan, and Fei-Yue Wang. Airvista-ii: An agentic system for embodied uavs toward dynamic scene semantic understanding. In 2025 IEEE International Conference on Systems, Man, and Cybernetics (SMC), pages 6319–6324, 2025.
- [18] Feng Yan, Fanfan Liu, Yiyang Huang, Zechao Guan, Liming Zheng, Yufeng Zhong, Chengjian Feng, and Lin Ma. Robotron-mani: All-in-one multimodal large model for robotic manipulation. In Proceedings of the IEEE/CVF International Conference on Computer Vision, pages 13707–13718, 2025.
- [19] Yingbo Tang, Lingfeng Zhang, Shuyi Zhang, Yinuo Zhao, and Xiaoshuai Hao. Roboafford: A dataset and benchmark for enhancing object and spatial affordance learning in robot manipulation. In Proceedings of the 33rd ACM International Conference on Multimedia, pages 12706–12713, 2025.
- [20] Yifu Yuan, Haiqin Cui, Yaoting Huang, Yibin Chen, Fei Ni, Zibin Dong, Pengyi Li, Yan Zheng, and Jianye Hao. Embodied-r1: Reinforced embodied reasoning for general robotic manipulation. arXiv preprint arXiv:2508.13998, 2025.
- [21] Dantong Niu, Yuvan Sharma, Giscard Biamby, Jerome Quenum, Yutong Bai, Baifeng Shi, Trevor Darrell, and Roei Herzig. Llarva: Vision-action instruction tuning enhances robot learning. arXiv preprint arXiv:2406.11815, 2024.
- [22] Yanbang Li, Ziyang Gong, Haoyang Li, Xiaoqi Huang, Haolan Kang, Guangping Bai, and Xianzheng Ma. Robotic visual instruction. In Proceedings of the Computer Vision and Pattern Recognition Conference, pages 12155–12165, 2025.
- [23] Naoki Wake, Atsushi Kanehira, Kazuhiro Sasabuchi, Jun Takamatsu, and Katsushi Ikeuchi. Gpt-4v (ision) for robotics: Multimodal task planning from human demonstration. IEEE Robotics and Automation Letters, 2024.
- [24] Chan Hee Song, Valts Blukis, Jonathan Tremblay, Stephen Tyree, Yu Su, and Stan Birchfield. Robospacial: Teaching spatial understanding to 2d and 3d vision-language models for robotics. In Proceedings of the Computer Vision and Pattern Recognition Conference, pages 15768–15780, 2025.
- [25] Delin Qu, Haoming Song, Qizhi Chen, Zhaoqing Chen, Xianqiang Gao, Xinyi Ye, Qi Lv, Modi Shi, Guanghui Ren, Cheng Ruan, Maoqing Yao, Haoran Yang, Jiacheng Bao, Bin Zhao, and Dong Wang. Eo-1: Interleaved vision-text-action pretraining for general robot control. arXiv preprint, 2025.
- [26] Gemini Team, Rohan Anil, Sebastian Borgeaud, Jean-Baptiste Alayrac, Jiahui Yu, Radu Soricut, Johan Schalkwyk, Andrew M Dai, Anja Hauth, Katie Millican, et al. Gemini: a family of highly capable multimodal models. arXiv preprint arXiv:2312.11805, 2023.
- [27] Wenyi Hong, Wenmeng Yu, Xiaotao Gu, Guo Wang, Guobing Gan, Haomiao Tang, Jiale Cheng, Ji Qi, Junhui Ji, Lihang Pan, et al. Glm-4.1 v-thinking: Towards versatile multimodal reasoning with scalable reinforcement learning. arXiv preprint arXiv:2507.01006, 2025.
- [28] Kimi Team, Tongtong Bai, Yifan Bai, Yiping Bao, SH Cai, Yuan Cao, Y Charles, HS Che, Cheng Chen, Guanduo Chen, et al. Kimi k2. 5: Visual agentic intelligence. arXiv preprint arXiv:2602.02276, 2026.
- [29] Junnan Li, Dongxu Li, Silvio Savarese, and Steven Hoi. Blip-2: Bootstrapping language-image pre-training with frozen image encoders and large language models. In International conference on machine learning, pages 19730–19742. PMLR, 2023.
- [30] Shuai Bai, Keqin Chen, Xuejing Liu, Jialin Wang, Wenbin Ge, Sibao Song, Kai Dang, Peng Wang, Shijie Wang, Jun Tang, et al. Qwen2. 5-vl technical report. arXiv preprint arXiv:2502.13923, 2025.
- [31] Peng Wang, Shuai Bai, Sinan Tan, Shijie Wang, Zhihao Fan, Jinze Bai, Keqin Chen, Xuejing Liu, Jialin Wang, Wenbin Ge, et al. Qwen2-vl: Enhancing vision-language model’s perception of the world at any resolution. arXiv preprint arXiv:2409.12191, 2024.
- [32] An Yang, Anfeng Li, Baosong Yang, Beichen Zhang, Binyuan Hui, Bo Zheng, Bowen Yu, Chang Gao, Chengen Huang, Chenxu Lv, et al. Qwen3 technical report. arXiv preprint arXiv:2505.09388, 2025.
- [33] Zhe Chen, Jiannan Wu, Wenhai Wang, Weijie Su, Guo Chen, Sen Xing, Muyan Zhong, Qinglong Zhang, Xizhou Zhu, Lewei Lu, et al. Internvl: Scaling up vision foundation models and aligning for generic visual-linguistic tasks. In Proceedings of the IEEE/CVF conference on computer vision and pattern recognition, pages 24185–24198, 2024.

- [34] Zhe Chen, Weiyun Wang, Yue Cao, Yangzhou Liu, Zhangwei Gao, Erfei Cui, Jinguo Zhu, Shenglong Ye, Hao Tian, Zhaoyang Liu, et al. Expanding performance boundaries of open-source multimodal models with model, data, and test-time scaling. [arXiv preprint arXiv:2412.05271](#), 2024.
- [35] Jinguo Zhu, Weiyun Wang, Zhe Chen, Zhaoyang Liu, Shenglong Ye, Lixin Gu, Hao Tian, Yuchen Duan, Weijie Su, Jie Shao, et al. Internvl3: Exploring advanced training and test-time recipes for open-source multimodal models. [arXiv preprint arXiv:2504.10479](#), 2025.
- [36] Weiyun Wang, Zhangwei Gao, Lixin Gu, Hengjun Pu, Long Cui, Xingguang Wei, Zhaoyang Liu, Linglin Jing, Shenglong Ye, Jie Shao, et al. Internvl3. 5: Advancing open-source multimodal models in versatility, reasoning, and efficiency. [arXiv preprint arXiv:2508.18265](#), 2025.
- [37] Shusheng Yang, Jihan Yang, Pinzhi Huang, Ellis Brown, Zihao Yang, Yue Yu, Shengbang Tong, Zihan Zheng, Yifan Xu, Muhan Wang, et al. Cambrian-s: Towards spatial supersensing in video. [arXiv preprint arXiv:2511.04670](#), 2025.
- [38] Zhongang Cai, Ruisi Wang, Chenyang Gu, Fanyi Pu, Junxiang Xu, Yubo Wang, Wanqi Yin, Zhitao Yang, Chen Wei, Qingping Sun, et al. Scaling spatial intelligence with multimodal foundation models. [arXiv preprint arXiv:2511.13719](#), 2025.
- [39] Zhongang Cai, Yubo Wang, Qingping Sun, Ruisi Wang, Chenyang Gu, Wanqi Yin, Zhiqian Lin, Zhitao Yang, Chen Wei, Oscar Qian, et al. Holistic evaluation of multimodal llms on spatial intelligence. [arXiv preprint arXiv:2508.13142](#), 2025.
- [40] Nianchen Deng, Lixin Gu, Shenglong Ye, Yinan He, Zhe Chen, Songze Li, Haomin Wang, Xingguang Wei, Tianshuo Yang, Min Dou, et al. Internspatial: A comprehensive dataset for spatial reasoning in vision-language models. [arXiv preprint arXiv:2506.18385](#), 2025.
- [41] Rui Yang, Ziyu Zhu, Yanwei Li, Jingjia Huang, Shen Yan, Siyuan Zhou, Zhe Liu, Xiangtai Li, Shuangye Li, Wenqian Wang, et al. Visual spatial tuning. [arXiv preprint arXiv:2511.05491](#), 2025.
- [42] Peiwen Sun, Shiqiang Lang, Dongming Wu, Yi Ding, Kaituo Feng, Huadai Liu, Zhen Ye, Rui Liu, Yun-Hui Liu, Jianan Wang, et al. Spacevista: All-scale visual spatial reasoning from mm to km. [arXiv preprint arXiv:2510.09606](#), 2025.
- [43] Ting Huang, Zeyu Zhang, and Hao Tang. 3d-r1: Enhancing reasoning in 3d vlms for unified scene understanding. [arXiv preprint arXiv:2507.23478](#), 2025.
- [44] Yuhong Liu, Beichen Zhang, Yuhang Zang, Yuhang Cao, Long Xing, Xiaoyi Dong, Haodong Duan, Dahua Lin, and Jiaqi Wang. Spatial-ssrl: Enhancing spatial understanding via self-supervised reinforcement learning. [arXiv preprint arXiv:2510.27606](#), 2025.
- [45] Runsen Xu, Weiyao Wang, Hao Tang, Xingyu Chen, Xiaodong Wang, Fu-Jen Chu, Dahua Lin, Matt Feiszli, and Kevin J Liang. Multi-spatialmlm: Multi-frame spatial understanding with multi-modal large language models. [arXiv preprint arXiv:2505.17015](#), 2025.
- [46] Jiangyong Huang, Xiaojian Ma, Xiongkun Linghu, Yue Fan, Junchao He, Wenxin Tan, Qing Li, Song-Chun Zhu, Yixin Chen, Baoxiong Jia, et al. Leo-vl: Towards 3d vision-language generalists via data scaling with efficient representation. [arXiv preprint arXiv:2506.09935](#), 2025.
- [47] Yi Han, Cheng Chi, Enshen Zhou, Shanyu Rong, Jingkun An, Pengwei Wang, Zhongyuan Wang, Lu Sheng, and Shanghang Zhang. Tiger: Tool-integrated geometric reasoning in vision-language models for robotics. [arXiv preprint arXiv:2510.07181](#), 2025.
- [48] Yuheng Ji, Huajie Tan, Jiayu Shi, Xiaoshuai Hao, Yuan Zhang, Hengyuan Zhang, Pengwei Wang, Mengdi Zhao, Yao Mu, Pengju An, et al. Robobrain: A unified brain model for robotic manipulation from abstract to concrete. In *Proceedings of the Computer Vision and Pattern Recognition Conference*, pages 1724–1734, 2025.
- [49] BAAI RoboBrain Team, Mingyu Cao, Huajie Tan, Yuheng Ji, Xiansheng Chen, Minglan Lin, Zhiyu Li, Zhou Cao, Pengwei Wang, Enshen Zhou, et al. Robobrain 2.0 technical report. [arXiv preprint arXiv:2507.02029](#), 2025.
- [50] Huajie Tan, Enshen Zhou, Zhiyu Li, Yijie Xu, Yuheng Ji, Xiansheng Chen, Cheng Chi, Pengwei Wang, Huizhu Jia, Yulong Ao, et al. Robobrain 2.5: Depth in sight, time in mind. [arXiv preprint arXiv:2601.14352](#), 2026.

- [51] Xiaoshuai Hao, Lei Zhou, Zhijian Huang, Zhiwen Hou, Yingbo Tang, Lingfeng Zhang, Guang Li, Zheng Lu, Shuhuai Ren, Xianhui Meng, et al. Mimo-embodied: X-embodied foundation model technical report. [arXiv preprint arXiv:2511.16518](#), 2025.
- [52] Ganlin Yang, Tianyi Zhang, Haoran Hao, Weiyun Wang, Yibin Liu, Dehui Wang, Guanzhou Chen, Zijian Cai, Junting Chen, Weijie Su, et al. Vlaser: Vision-language-action model with synergistic embodied reasoning. [arXiv preprint arXiv:2510.11027](#), 2025.
- [53] Gen Luo, Ganlin Yang, Ziyang Gong, Guanzhou Chen, Haonan Duan, Erfei Cui, Ronglei Tong, Zhi Hou, Tianyi Zhang, Zhe Chen, et al. Visual embodied brain: Let multimodal large language models see, think, and control in spaces. [arXiv preprint arXiv:2506.00123](#), 2025.
- [54] Yi Zhang, Che Liu, Xiancong Ren, Hanchu Ni, Shuai Zhang, Zeyuan Ding, Jiayu Hu, Hanzhe Shan, Zhenwei Niu, Zhaoyang Liu, et al. Pelican-vl 1.0: A foundation brain model for embodied intelligence. [arXiv preprint arXiv:2511.00108](#), 2025.
- [55] NVIDIA, Alisson Azzolini, Hannah Brandon, Prithvijit Chattopadhyay, Huayu Chen, Jinju Chu, Yin Cui, Jenna Diamond, Yifan Ding, Francesco Ferroni, Rama Govindaraju, Jinwei Gu, Siddharth Gururani, Imad El Hanafi, Zekun Hao, Jacob Huffman, Jingyi Jin, Brendan Johnson, Rizwan Khan, George Kurian, Elena Lantz, Nayeon Lee, Zhaoshuo Li, Xuan Li, Tsung-Yi Lin, Yen-Chen Lin, Ming-Yu Liu, Andrew Mathau, Yun Ni, Lindsey Pavao, Wei Ping, David W. Romero, Misha Smelyanskiy, Shuran Song, Lyne Tchapmi, Andrew Z. Wang, Boxin Wang, Haoxiang Wang, Fangyin Wei, Jiashu Xu, Yao Xu, Xiaodong Yang, Zhuolin Yang, Xiaohui Zeng, and Zhe Zhang. Cosmos-reason1: From physical common sense to embodied reasoning, 2025.
- [56] Huang Fang, Mengxi Zhang, Heng Dong, Zixuan Wang, Wei Li, Qifeng Zhang, Xueyun Tian, Yucheng Hu, and Hang Li. Robix: A Unified Model for Robot Interaction, Reasoning and Planning. [arXiv preprint arXiv:2509.01106](#), 2025.
- [57] Yaru Cao, Zhijian He, Lujia Wang, Wenguan Wang, Yixuan Yuan, Dingwen Zhang, Jinglin Zhang, Pengfei Zhu, Luc Van Gool, Junwei Han, et al. Visdrone-det2021: The vision meets drone object detection challenge results. In [Proceedings of the IEEE/CVF International conference on computer vision](#), pages 2847–2854, 2021.
- [58] Xin Zhou, Zhepei Wang, Hongkai Ye, Chao Xu, and Fei Gao. Ego-planner: An esdf-free gradient-based local planner for quadrotors. [IEEE Robotics and Automation Letters](#), 6(2):478–485, 2021.
- [59] Yue Zhou, Litong Feng, Mengcheng Lan, Xue Yang, Qingyun Li, Yiping Ke, Xue Jiang, and Wayne Zhang. Multimodal mathematical reasoning embedded in aerial vehicle imagery: Benchmarking, analysis, and exploration. [ISPRS Journal of Photogrammetry and Remote Sensing](#), 230:289–303, 2025.
- [60] Huazi Cao, Jiahao Shen, Yin Zhang, Zheng Fu, Cunjia Liu, Sihao Sun, and Shiyu Zhao. Proximal cooperative aerial manipulation with vertically stacked drones. [Nature](#), 646(8085):576–583, 2025.
- [61] Yifan Wang, Jian Zhao, Zhaoxin Fan, Xin Zhang, Xuecheng Wu, Yudian Zhang, Lei Jin, Xinyue Li, Gang Wang, Mengxi Jia, et al. Jtd-uav: Mllm-enhanced joint tracking and description framework for anti-uav systems. In [Proceedings of the Computer Vision and Pattern Recognition Conference](#), pages 1633–1644, 2025.
- [62] Meng Chu, Zhedong Zheng, Wei Ji, Tingyu Wang, and Tat-Seng Chua. Towards natural language-guided drones: Geotext-1652 benchmark with spatial relation matching. In [European Conference on Computer Vision](#), pages 213–231. Springer, 2024.
- [63] Lingfeng Zhang, Yuchen Zhang, Hongsheng Li, Haoxiang Fu, Yingbo Tang, Hangjun Ye, Long Chen, Xiaojun Liang, Xiaoshuai Hao, and Wenbo Ding. Is your vlm sky-ready? a comprehensive spatial intelligence benchmark for uav navigation. [arXiv preprint arXiv:2511.13269](#), 2025.
- [64] Mingning Guo, Mengwei Wu, Jiarun He, Shaoxian Li, Haifeng Li, and Chao Tao. Bedi: A comprehensive benchmark for evaluating embodied agents on uavs. [arXiv preprint arXiv:2505.18229](#), 2025.
- [65] Xiangyu Wang, Donglin Yang, Yue Liao, Wenhao Zheng, Bin Dai, Hongsheng Li, Si Liu, et al. Uav-flow colosseo: A real-world benchmark for flying-on-a-word uav imitation learning. [arXiv preprint arXiv:2505.15725](#), 2025.
- [66] Fanglong Yao, Yuanchang Yue, Youzhi Liu, Xian Sun, and Kun Fu. Aeroverse: Uav-agent benchmark suite for simulating, pre-training, finetuning, and evaluating aerospace embodied world models. [arXiv preprint arXiv:2408.15511](#), 2024.

- [67] Arijit Ray, Jiafei Duan, Ellis Brown, Reuben Tan, Dina Bashkirova, Rose Hendrix, Kiana Ehsani, Aniruddha Kembhavi, Bryan A Plummer, Ranjay Krishna, et al. Sat: Dynamic spatial aptitude training for multimodal language models. *arXiv preprint arXiv:2412.07755*, 2024.
- [68] Baiqiao Yin, Qineng Wang, Pingyue Zhang, Jianshu Zhang, Kangrui Wang, Zihan Wang, Jieyu Zhang, Keshigeyan Chandrasegaran, Han Liu, Ranjay Krishna, et al. Spatial mental modeling from limited views. In *Structural Priors for Vision Workshop at ICCV’25*, 2025.
- [69] Yi-Fan Zhang, Huanyu Zhang, Haochen Tian, Chaoyou Fu, Shuangqing Zhang, Junfei Wu, Feng Li, Kun Wang, Qingsong Wen, Zhang Zhang, et al. Mme-realworld: Could your multimodal llm challenge high-resolution real-world scenarios that are difficult for humans? *arXiv preprint arXiv:2408.13257*, 2024.
- [70] Sung-Yeon Park, Can Cui, Yunsheng Ma, Ahmadreza Moradipari, Rohit Gupta, Kyungtae Han, and Ziran Wang. Nuplanqa: A large-scale dataset and benchmark for multi-view driving scene understanding in multi-modal large language models. *arXiv preprint arXiv:2503.12772*, 2025.
- [71] Shuai Bai, Yuxuan Cai, Ruizhe Chen, Keqin Chen, Xionghui Chen, Zesen Cheng, Lianghao Deng, Wei Ding, Chang Gao, Chunjiang Ge, Wenbin Ge, Zhifang Guo, Qidong Huang, Jie Huang, Fei Huang, Binyuan Hui, Shutong Jiang, Zhaohai Li, Mingsheng Li, Mei Li, Kaixin Li, Zicheng Lin, Junyang Lin, Xuejing Liu, Jiawei Liu, Chenglong Liu, Yang Liu, Dayiheng Liu, Shixuan Liu, Dunjie Lu, Ruilin Luo, Chenxu Lv, Rui Men, Lingchen Meng, Xuancheng Ren, Xingzhang Ren, Sibao Song, Yuchong Sun, Jun Tang, Jianhong Tu, Jianqiang Wan, Peng Wang, Pengfei Wang, Qiuyue Wang, Yuxuan Wang, Tianbao Xie, Yiheng Xu, Haiyang Xu, Jin Xu, Zhibo Yang, Mingkun Yang, Jianxin Yang, An Yang, Bowen Yu, Fei Zhang, Hang Zhang, Xi Zhang, Bo Zheng, Humen Zhong, Jingren Zhou, Fan Zhou, Jing Zhou, Yuanzhi Zhu, and Ke Zhu. Qwen3-vl technical report. *arXiv preprint arXiv:2511.21631*, 2025.
- [72] Peter Tong, Ellis Brown, Penghao Wu, Sanghyun Woo, Adithya Jairam Vedagiri IYER, Sai Charitha Akula, Shusheng Yang, Jihan Yang, Manoj Middepogu, Ziteng Wang, et al. Cambrian-1: A fully open, vision-centric exploration of multimodal llms. *Advances in Neural Information Processing Systems*, 37:87310–87356, 2024.
- [73] Enneng Yang, Zhenyi Wang, Li Shen, Shiwei Liu, Guibing Guo, Xingwei Wang, and Dacheng Tao. Adamerging: Adaptive model merging for multi-task learning. In *The Twelfth International Conference on Learning Representations*, 2024.
- [74] Li Shen, Anke Tang, Enneng Yang, Guibing Guo, Yong Luo, Lefei Zhang, Xiaochun Cao, Bo Du, and Dacheng Tao. Efficient and effective weight-ensembling mixture of experts for multi-task model merging. *IEEE Transactions on Pattern Analysis and Machine Intelligence*, 2025.
- [75] Runxi Cheng, Feng Xiong, Yongxian Wei, Wanyun Zhu, and Chun Yuan. Whoever Started the interference Should End It: Guiding Data-Free Model Merging via Task Vectors. In *Proceedings of the 42nd International Conference on Machine Learning*, pages 10121–10143. PMLR, 2025.
- [76] Yongxian Wei, Runxi Cheng, WeiKe Jin, Enneng Yang, Li Shen, Lu Hou, Sinan Du, Chun Yuan, Xiaochun Cao, and Dacheng Tao. Unifying multimodal large language model capabilities and modalities via model merging. *arXiv preprint arXiv:2505.19892*, 2025.
- [77] Anke Tang, Li Shen, Yong Luo, Enneng Yang, Han Hu, Lefei Zhang, Bo Du, and Dacheng Tao. Fusionbench: A unified library and comprehensive benchmark for deep model fusion. *arXiv preprint arXiv:2406.03280*, 2025.
- [78] Antonio Andrea Gargiulo, Donato Crisostomi, Maria Sofia Bucarelli, Simone Scardapane, Fabrizio Silvestri, and Emanuele Rodola. Task singular vectors: Reducing task interference in model merging. In *Proceedings of the Computer Vision and Pattern Recognition Conference*, pages 18695–18705, 2025.
- [79] Mitchell Wortsman, Gabriel Ilharco, Samir Ya Gadre, Rebecca Roelofs, Raphael Gontijo-Lopes, Ari S Morcos, Hongseok Namkoong, Ali Farhadi, Yair Carmon, Simon Kornblith, et al. Model soups: averaging weights of multiple fine-tuned models improves accuracy without increasing inference time. In *International conference on machine learning*, pages 23965–23998. PMLR, 2022.
- [80] Atoosa Chegini, Hamid Kazemi, Seyed Iman Mirzadeh, Dong Yin, Maxwell Horton, Moin Nabi, Mehrdad Farajtabar, and Keivan Alizadeh. Model soup for better rlhf: Weight space averaging to improve alignment in llms. In *NeurIPS 2024 Workshop on Fine-Tuning in Modern Machine Learning: Principles and Scalability*, 2024.

- [81] Zhihong Shao, Peiyi Wang, Qihao Zhu, Runxin Xu, Junxiao Song, Xiao Bi, Haowei Zhang, Mingchuan Zhang, Y. K. Li, Y. Wu, and Daya Guo. Deepseekmath: Pushing the limits of mathematical reasoning in open language models, 2024.
- [82] Jihan Yang, Shusheng Yang, Anjali W Gupta, Rilyn Han, Li Fei-Fei, and Saining Xie. Thinking in space: How multimodal large language models see, remember, and recall spaces. In Proceedings of the Computer Vision and Pattern Recognition Conference, pages 10632–10643, 2025.
- [83] Sihan Yang, Runsen Xu, Yiman Xie, Sizhe Yang, Mo Li, Jingli Lin, Chenming Zhu, Xiaochen Chen, Haodong Duan, Xiangyu Yue, et al. Mmsi-bench: A benchmark for multi-image spatial intelligence. arXiv preprint arXiv:2505.23764, 2025.
- [84] Xingyu Fu, Yushi Hu, Bangzheng Li, Yu Feng, Haoyu Wang, Xudong Lin, Dan Roth, Noah A Smith, Wei-Chiu Ma, and Ranjay Krishna. Blink: Multimodal large language models can see but not perceive. In European Conference on Computer Vision, pages 148–166. Springer, 2024.
- [85] Wenqi Wang, Reuben Tan, Pengyue Zhu, Jianwei Yang, Zhengyuan Yang, Lijuan Wang, Andrey Kolobov, Jianfeng Gao, and Boqing Gong. Site: towards spatial intelligence thorough evaluation. In Proceedings of the IEEE/CVF International Conference on Computer Vision, pages 9058–9069, 2025.
- [86] Yiming Zhang, ZeMing Gong, and Angel X Chang. Multi3drefer: Grounding text description to multiple 3d objects. In Proceedings of the IEEE/CVF International Conference on Computer Vision, pages 15225–15236, 2023.
- [87] OpenAI. Gpt-4o system card. <https://openai.com/index/gpt-4o-system-card/>, 2025.
- [88] Anthropic. Claude sonnet 4. 2025.
- [89] Core Team, Zihao Yue, Zhenru Lin, Yifan Song, Weikun Wang, Shuhuai Ren, Shuhao Gu, Shicheng Li, Peidian Li, Liang Zhao, Lei Li, Kainan Bao, Hao Tian, Hailin Zhang, Gang Wang, Dawei Zhu, Cici, Chenhong He, Bowen Ye, Bowen Shen, Zihan Zhang, Zihan Jiang, Zhixian Zheng, Zhichao Song, Zhenbo Luo, Yue Yu, Yudong Wang, Yuanyuan Tian, Yu Tu, Yihan Yan, Yi Huang, Xu Wang, Xinzhe Xu, Xingchen Song, Xing Zhang, Xing Yong, Xin Zhang, Xiangwei Deng, Wenyu Yang, Wenhan Ma, Weiwei Lv, Weiji Zhuang, Wei Liu, Sirui Deng, Shuo Liu, Shimao Chen, Shihua Yu, Shaohui Liu, Shande Wang, Rui Ma, Qiantong Wang, Peng Wang, Nuo Chen, Menghang Zhu, Kangyang Zhou, Kang Zhou, Kai Fang, Jun Shi, Jinhao Dong, Jiebao Xiao, Jiaming Xu, Huaqiu Liu, Hongshen Xu, Heng Qu, Haochen Zhao, Hanglong Lv, Guoan Wang, Duo Zhang, Dong Zhang, Di Zhang, Chong Ma, Chang Liu, Can Cai, and Bingquan Xia. Mimo-vl technical report, 2025.
- [90] Xu Cao, Tong Zhou, Yunsheng Ma, Wenqian Ye, Can Cui, Kun Tang, Zhipeng Cao, Kaizhao Liang, Ziran Wang, James M Rehg, et al. Maplm: A real-world large-scale vision-language benchmark for map and traffic scene understanding. In Proceedings of the IEEE/CVF conference on computer vision and pattern recognition, pages 21819–21830, 2024.
- [91] Yuhan Hao, Zhengning Li, Lei Sun, Weilong Wang, Naixin Yi, Sheng Song, Caihong Qin, Mofan Zhou, Yifei Zhan, and Xianpeng Lang. Driveaction: A benchmark for exploring human-like driving decisions in vla models. arXiv preprint arXiv:2506.05667, 2025.
- [92] Tianwen Qian, Jingjing Chen, Linhai Zhuo, Yang Jiao, and Yu-Gang Jiang. Nuscenes-qa: A multi-modal visual question answering benchmark for autonomous driving scenario. In Proceedings of the AAAI Conference on Artificial Intelligence, volume 38, pages 4542–4550, 2024.
- [93] Ana-Maria Marcu, Long Chen, Jan Hünermann, Alice Karnsund, Benoit Hanotte, Prajwal Chidananda, Saurabh Nair, Vijay Badrinarayanan, Alex Kendall, Jamie Shotton, et al. Lingoqa: Visual question answering for autonomous driving. In European Conference on Computer Vision, pages 252–269. Springer, 2024.
- [94] Kun Li, George Vosselman, and Michael Ying Yang. Hrvqa: A visual question answering benchmark for high-resolution aerial images. ISPRS Journal of Photogrammetry and Remote Sensing, 214:65–81, 2024.
- [95] Gemini Robotics Team, Saminda Abeyruwan, Joshua Ainslie, Jean-Baptiste Alayrac, Montserrat Gonzalez Arenas, Travis Armstrong, Ashwin Balakrishna, Robert Baruch, Maria Bauza, Michiel Blokzijl, et al. Gemini robotics: Bringing ai into the physical world. arXiv preprint arXiv:2503.20020, 2025.
- [96] Pierre Sermanet, Tianli Ding, Jeffrey Zhao, Fei Xia, Debidatta Dwibedi, Keerthana Gopalakrishnan, Christine Chan, Gabriel Dulac-Arnold, Sharath Maddineni, Nikhil J Joshi, et al. Robovqa: Multimodal long-horizon

- reasoning for robotics. In 2024 IEEE International Conference on Robotics and Automation (ICRA), pages 645–652. IEEE, 2024.
- [97] Arjun Majumdar, Anurag Ajay, Xiaohan Zhang, Pranav Putta, Sriram Yenamandra, Mikael Henaff, Sneha Silwal, Paul Mcvay, Oleksandr Maksymets, Sergio Arnaud, et al. Openeqa: Embodied question answering in the era of foundation models. In Proceedings of the IEEE/CVF conference on computer vision and pattern recognition, pages 16488–16498, 2024.
- [98] Mengfei Du, Binhao Wu, Zejun Li, Xuan-Jing Huang, and Zhongyu Wei. Embspatial-bench: Benchmarking spatial understanding for embodied tasks with large vision-language models. In Proceedings of the 62nd Annual Meeting of the Association for Computational Linguistics (Volume 2: Short Papers), pages 346–355, 2024.
- [99] Yi Chen, Yuying Ge, Yixiao Ge, Mingyu Ding, Bohao Li, Rui Wang, Ruifeng Xu, Ying Shan, and Xihui Liu. Egoplan-bench: Benchmarking egocentric embodied planning with multimodal large language models. CoRR, 2023.
- [100] Rui Yang, Hanyang Chen, Junyu Zhang, Mark Zhao, Cheng Qian, Kangrui Wang, Qineng Wang, Teja Venkat Koripella, Marziyeh Movahedi, Manling Li, et al. Embodiedbench: Comprehensive benchmarking multi-modal large language models for vision-driven embodied agents. arXiv preprint arXiv:2502.09560, 2025.
- [101] Haotian Liu, Chunyuan Li, Yuheng Li, and Yong Jae Lee. Improved baselines with visual instruction tuning. In Proceedings of the IEEE/CVF conference on computer vision and pattern recognition, pages 26296–26306, 2024.
- [102] Matt Deitke, Eli VanderBilt, Alvaro Herrasti, Luca Weihs, Jordi Salvador, Kiana Ehsani, Winson Han, Eric Kolve, Ali Farhadi, Aniruddha Kembhavi, et al. Proctor: Large-scale embodied ai using procedural generation. arXiv preprint arXiv:2206.06994, 2022.
- [103] Qi Feng. Visuospatial cognitive assistant. arXiv preprint arXiv:2505.12312, 2025.
- [104] Zhangyang Qi, Zhixiong Zhang, Ye Fang, Jiaqi Wang, and Hengshuang Zhao. Gpt4scene: Understand 3d scenes from videos with vision-language models. arXiv preprint arXiv:2501.01428, 2025.
- [105] Ting Huang, Zeyu Zhang, and Hao Tang. 3d-r1: Enhancing reasoning in 3d vlms for unified scene understanding. arXiv preprint arXiv:2507.23478, 2025.
- [106] Zhiwen Fan, Jian Zhang, Renjie Li, Junge Zhang, Runjin Chen, Hezhen Hu, Kevin Wang, Huaizhi Qu, Dilin Wang, Zhicheng Yan, et al. Vlm-3r: Vision-language models augmented with instruction-aligned 3d reconstruction. arXiv preprint arXiv:2505.20279, 2025.
- [107] Angela Dai, Angel X Chang, Manolis Savva, Maciej Halber, Thomas Funkhouser, and Matthias Nießner. Scannet: Richly-annotated 3d reconstructions of indoor scenes. In Proceedings of the IEEE conference on computer vision and pattern recognition, pages 5828–5839, 2017.
- [108] Chandan Yeshwanth, Yueh-Cheng Liu, Matthias Nießner, and Angela Dai. Scannet++: A high-fidelity dataset of 3d indoor scenes. In Proceedings of the IEEE/CVF International Conference on Computer Vision, pages 12–22, 2023.
- [109] Gilad Baruch, Zhuoyuan Chen, Afshin Dehghan, Tal Dimry, Yuri Feigin, Peter Fu, Thomas Gebauer, Brandon Joffe, Daniel Kurz, Arik Schwartz, et al. Arkitscenes: A diverse real-world dataset for 3d indoor scene understanding using mobile rgb-d data. arXiv preprint arXiv:2111.08897, 2021.
- [110] Angel Chang, Angela Dai, Thomas Funkhouser, Maciej Halber, Matthias Niessner, Manolis Savva, Shuran Song, Andy Zeng, and Yinda Zhang. Matterport3d: Learning from rgb-d data in indoor environments. arXiv preprint arXiv:1709.06158, 2017.
- [111] Kun Ouyang, Yuanxin Liu, Haoning Wu, Yi Liu, Hao Zhou, Jie Zhou, Fandong Meng, and Xu Sun. Spacer: Reinforcing mllms in video spatial reasoning. arXiv preprint arXiv:2504.01805, 2025.
- [112] Xu Cao, Tong Zhou, Yunsheng Ma, Wenqian Ye, Can Cui, Kun Tang, Zhipeng Cao, Kaizhao Liang, Ziran Wang, James M Rehg, et al. Maplm: A real-world large-scale vision-language benchmark for map and traffic scene understanding. In Proceedings of the IEEE/CVF conference on computer vision and pattern recognition, pages 21819–21830, 2024.

- [113] Yuhan Hao, Zhengning Li, Lei Sun, Weilong Wang, Naixin Yi, Sheng Song, Caihong Qin, Mofan Zhou, Yifei Zhan, and Xianpeng Lang. Driveaction: A benchmark for exploring human-like driving decisions in vla models. [arXiv preprint arXiv:2506.05667](#), 2025.
- [114] Tianwen Qian, Jingjing Chen, Linhai Zhuo, Yang Jiao, and Yu-Gang Jiang. Nuscenes-qa: A multi-modal visual question answering benchmark for autonomous driving scenario. In [Proceedings of the AAAI Conference on Artificial Intelligence](#), volume 38, pages 4542–4550, 2024.
- [115] Ana-Maria Marcu, Long Chen, Jan Hünermann, Alice Karnsund, Benoit Hanotte, Prajwal Chidananda, Saurabh Nair, Vijay Badrinarayanan, Alex Kendall, Jamie Shotton, et al. Lingoqa: Visual question answering for autonomous driving. In [European Conference on Computer Vision](#), pages 252–269. Springer, 2024.
- [116] Weichen Zhang, Zile Zhou, Xin Zeng, Liu Xuchen, Jianjie Fang, Chen Gao, Jinqiang Cui, Yong Li, Xinlei Chen, and Xiao-Ping Zhang. Open3d-vqa: A benchmark for embodied spatial concept reasoning with multimodal large language model in open space. In [Proceedings of the 33rd ACM International Conference on Multimedia](#), pages 12784–12791, 2025.
- [117] Jirong Zha, Yuxuan Fan, Tianyu Zhang, Geng Chen, Yingfeng Chen, Chen Gao, and Xinlei Chen. Aircopbench: A benchmark for multi-drone collaborative embodied perception and reasoning. [arXiv preprint arXiv:2511.11025](#), 2025.
- [118] Laila Bashmal, Yakoub Bazi, Mohamad Mahmoud Al Rahhal, Mansour Zuair, and Farid Melgani. Capera: Captioning events in aerial videos. [Remote Sensing](#), 15(8):2139, 2023.
- [119] Kanxue Li, Baosheng Yu, Qi Zheng, Yibing Zhan, Yuhui Zhang, Tianle Zhang, Yijun Yang, Yue Chen, Lei Sun, Qiong Cao, Li Shen, Lusong Li, Dapeng Tao, and Xiaodong He. Muep: A multimodal benchmark for embodied planning with foundation models. In Kate Larson, editor, [Proceedings of the Thirty-Third International Joint Conference on Artificial Intelligence, IJCAI-24](#), pages 129–138. International Joint Conferences on Artificial Intelligence Organization, 8 2024. Main Track.
- [120] Junting Chen, Haotian Liang, Lingxiao Du, Weiyun Wang, Mengkang Hu, Yao Mu, Wenhai Wang, Jifeng Dai, Ping Luo, Wenqi Shao, et al. Owmm-agent: Open world mobile manipulation with multi-modal agentic data synthesis. [arXiv preprint arXiv:2506.04217](#), 2025.
- [121] Junhao Shi, Zhaoye Fei, Siyin Wang, Qipeng Guo, Jingjing Gong, and Xipeng Qiu. World-aware planning narratives enhance large vision-language model planner, 2025.
- [122] Andrew Szot, Max Schwarzer, Harsh Agrawal, Bogdan Mazouze, Rin Metcalf, Walter Talbott, Natalie Mackraz, R Devon Hjelm, and Alexander T Toshev. Large language models as generalizable policies for embodied tasks. In [The Twelfth International Conference on Learning Representations](#), 2024.
- [123] Kaiyuan Chen, Shuangyu Xie, Zehan Ma, Pannag R Sanketi, and Ken Goldberg. Robo2vlm: Visual question answering from large-scale in-the-wild robot manipulation datasets. [arXiv preprint arXiv:2505.15517](#), 2025.
- [124] Yao Mu, Qinglong Zhang, Mengkang Hu, Wenhai Wang, Mingyu Ding, Jun Jin, Bin Wang, Jifeng Dai, Yu Qiao, and Ping Luo. EmbodiedGPT: Vision-language pre-training via embodied chain of thought. In [Thirty-seventh Conference on Neural Information Processing Systems](#), 2023.
- [125] Kaichen Zhang, Bo Li, Peiyuan Zhang, Fanyi Pu, Joshua Adrian Cahyono, Kairui Hu, Shuai Liu, Yuanhan Zhang, Jingkang Yang, Chunyuan Li, et al. Lmms-eval: Reality check on the evaluation of large multimodal models. In [Findings of the Association for Computational Linguistics: NAACL 2025](#), pages 881–916, 2025.
- [126] Andrew Szot, Alexander Clegg, Eric Undersander, Erik Wijmans, Yili Zhao, John Turner, Noah Maestre, Mustafa Mukadam, Devendra Singh Chaplot, Oleksandr Maksymets, Aaron Gokaslan, Vladimír Vondruš, Sameer Dharur, Franziska Meier, Wojciech Galuba, Angel Chang, Zsolt Kira, Vladlen Koltun, Jitendra Malik, Manolis Savva, and Dhruv Batra. Habitat 2.0: Training home assistants to rearrange their habitat. In M. Ranzato, A. Beygelzimer, Y. Dauphin, P.S. Liang, and J. Wortman Vaughan, editors, [Advances in Neural Information Processing Systems](#), volume 34, pages 251–266. Curran Associates, Inc., 2021.
- [127] Marianne Fyhn, Sturla Molden, Menno P Witter, Edvard I Moser, and May-Britt Moser. Spatial representation in the entorhinal cortex. [Science](#), 305(5688):1258–1264, 2004.
- [128] Torkel Hafting, Marianne Fyhn, Sturla Molden, May-Britt Moser, and Edvard I Moser. Microstructure of a spatial map in the entorhinal cortex. [Nature](#), 436(7052):801–806, 2005.

- [129] Kaixi Tian, Zhiping Zhao, Yang Chen, Ningling Ge, Shenghao Cao, Xinyong Han, Jianwen Gu, and Shan Yu. Domain-specific schema reuse supports flexible learning to learn in the primate brain. Nature Communications, 2026.
- [130] Vishwa Goudar, Barbara Peysakhovich, David J Freedman, Elizabeth A Buffalo, and Xiao-Jing Wang. Schema formation in a neural population subspace underlies learning-to-learn in flexible sensorimotor problem-solving. Nature Neuroscience, 26(5):879–890, 2023.
- [131] Shai Shalev-Shwartz and Shai Ben-David. Understanding machine learning: From theory to algorithms. Cambridge university press, 2014.
- [132] Mehryar Mohri, Afshin Rostamizadeh, and Ameet Talwalkar. Foundations of machine learning. MIT press, 2018.
- [133] Kaiyang Zhou, Ziwei Liu, Yu Qiao, Tao Xiang, and Chen Change Loy. Domain generalization: A survey. IEEE transactions on pattern analysis and machine intelligence, 45(4):4396–4415, 2022.

A Appendix

A.1 Mathematical Foundations of the Spatial Scaffold Mechanism

Notation. Let $\mathcal{M} = \{m_1, \dots, m_K\}$ denote a set of morphologies. Each morphology $m \in \mathcal{M}$ induces a data distribution D_m over tuples (o, c, y) , where $o \in \mathcal{O}_m$ represents multimodal observations, $c \in \mathcal{C}$ denotes task conditioning, and $y \in \mathcal{Y}_m$ is the target output. We evaluate the generalization performance on morphology m via the expected risk:

$$R_m(\theta) := \mathbb{E}_{(o,c,y) \sim D_m} [\ell_\theta(o, c, y)].$$

We further define the gradient of the risk as

$$g_m(\theta) := \nabla_\theta R_m(\theta).$$

The per-sample loss is defined as the negative log-likelihood under an autoregressive model:

$$\ell_\theta(o, c, y) := -\log p_\theta(y | o, c), \quad \text{where} \quad p_\theta(y | o, c) = \prod_{t=1}^T p_\theta(y_t | y_{<t}, o, c),$$

which yields the equivalent form:

$$\ell_\theta(o, c, y) = -\sum_{t=1}^T \log p_\theta(y_t | y_{<t}, o, c).$$

Let θ_{base} denote the base model. During the isolation stage, we obtain an expert θ_m for each morphology m . We then define the *task vector* as

$$\tau_m := \theta_m - \theta_{\text{base}}.$$

Adopting a layer-wise decomposition with L layers, we denote $\theta_m = (\theta_{m,1}, \dots, \theta_{m,L})$ and $\tau_m = (\tau_{m,1}, \dots, \tau_{m,L})$, where $\tau_{m,l} := \theta_{m,l} - \theta_{\text{base},l}$ for each layer $l \in \{1, \dots, L\}$.

Shared geometric scaffold as a universal spatial bridge. We interpret spatial intelligence as the ability to infer and reuse a morphology-invariant spatial scaffold across diverse embodiments. Concretely, there exists a shared latent spatial variable $g \in \mathcal{G}$ that captures 3D spatial relationships (layout, relative pose, depth, topology) and remains invariant across morphologies, and a morphology-specific latent $a_m \in \mathcal{A}_m$ that captures embodiment-dependent factors (sensor intrinsics, dynamics constraints, actuation semantics). For samples $(o, c, y) \sim D_m$, we posit the mechanism

$$o = \Psi_m(g, a_m), \quad y = \Phi(g, c),$$

where $g \sim P_G$ and $a_m \sim P_{A|m}$. Thus g serves as a **universal bridge** for cross-embodiment transfer, while morphology-specific variation is absorbed by Ψ_m and a_m .

Assumption 1 (Recoverable spatial scaffold representation after SCAFFOLD). *Let θ_{spatial} denote the parameters after the SCAFFOLD stage and define the induced representation $z_{\text{sp}} := h_{\theta_{\text{spatial}}}(o, c)$, where $o \in \mathcal{O}_m$ and $c \in \mathcal{C}$. There exist a decoder $\text{Dec}(\cdot)$ and a constant $\varepsilon_g \geq 0$ such that*

$$\mathbb{E} \left[\left\| \text{Dec}(z_{\text{sp}}) - g \right\| \right] \leq \varepsilon_g.$$

Assumption 1 is well founded because it formalizes a decodability property that serves as the primary objective of the Scaffold stage. By making geometric information readable from the representation, the shared scaffold g becomes a stable and transferable spatial core. Consequently, downstream learning remains focused on morphology specific factors rather than the redundant re-learning of geometry. The low recoverability error ε_g is empirically supported by functional decodability where the Spatial Expert demonstrates a marked improvement on spatial benchmarks from a baseline of 51.6 \rightarrow 72.5. This spatial foundation catalyzes learning in other morphologies as seen in the substantial gains for autonomous driving and aerial tasks when initialized from the spatial model. These results indicate the effective reuse of a shared scaffold instead of task specific overfitting. This concept also aligns with neuroscientific findings regarding reusable internal spatial codes that remain readable despite changing sensory conditions as described in Remark 2.

Remark 1. *Assumption 1 states that SCAFFOLD training induces a reusable representation from which the shared spatial scaffold g can be reliably recovered (up to error ε_g). This makes g a stable, transferable spatial core across morphologies, and isolates subsequent adaptation to morphology-specific factors rather than relearning geometry.*

Remark 2 (Neuroscientific evidence supporting reusable spatial scaffolds and representation space separation). *The mechanistic interpretation of SCAFFOLD treats g as a morphology-invariant spatial scaffold supporting decision-relevant reasoning while morphology-dependent factors are absorbed by the mapping Ψ_m . This perspective is strongly supported by two primary lines of neuroscientific evidence.*

First, research on hippocampal and entorhinal systems suggests that mammals maintain an internal and reusable spatial coordinate representation. This mechanism is frequently identified as an internal global positioning system that enables localization and navigation across changing sensory conditions. Such biological findings provide a foundation for a shared geometry-like variable g serving as a cross-domain substrate for planning and spatial reasoning [127, 128].

Second, population-level recordings and modeling studies indicate that reusable task structures are organized in stable low-dimensional subspaces which remain nearly separable from context-specific or stimulus-specific variation. For example, recent primate recordings identify decision-related and stimulus-related subspaces with a near-orthogonal relationship. In this framework, the reuse of schema-like patterns in the decision subspace facilitates subsequent learning and reduces cross-domain interference [129]. Complementary evidence shows that reusable schemas emerge within low-dimensional subspaces of population activity. The reuse of such schemas in new problems accelerates learning by limiting weight changes [130]. These empirical results motivate the emphasis on geometric recoverability. Specifically, SCAFFOLD aims to induce a representation $h_{\theta_{\text{spatial}}}$ from which g is reliably decodable so that downstream adaptation can focus on morphology-specific factors rather than relearning the shared spatial core.

A.2 Gradient Interference and the Necessity of Isolation Training

This subsection formalizes a key obstacle in joint cross-morphology training: gradients from different morphologies can be misaligned, so a single shared update may fail to simultaneously decrease all morphology-specific risks. We show that negative cross-gradient inner products naturally quantify such interference, which slows down, stalls, or even reverses progress on some morphologies. This provides a theoretical justification for isolation training, which removes cross-terms by construction.

Assumption 2 (Smoothness). *For each $m \in \mathcal{M}$, the risk $R_m(\theta)$ is L -smooth: for all θ, θ' ,*

$$R_m(\theta') \leq R_m(\theta) + \langle g_m(\theta), \theta' - \theta \rangle + \frac{L}{2} \|\theta' - \theta\|^2. \quad (12)$$

Assumption 2 is appropriate because the training setup utilizes the Adam optimizer with a modest learning rate coupled with robust stabilizers such as gradient clipping and weight decay. Such measures ensure that parameter updates remain within a locally well-behaved region where the objective function is effectively approximated as nearly quadratic. Under these conditions it is reasonable to upper bound the local curvature with a single smoothness constant L . Additionally, L smoothness is a standard regularity assumption in the field of optimization and is frequently adopted to formulate stability arguments for gradient-based approaches [131, 132].

Theorem 1 (One-step interference bound). *Let $w \in \Delta_K$ be nonnegative weights, and define the joint risk $R_w(\theta) := \sum_{j=1}^K w_j R_j(\theta)$. Consider one shared update*

$$\theta^+ = \theta - \eta \nabla R_w(\theta) = \theta - \eta \sum_{j=1}^K w_j g_j(\theta). \quad (13)$$

Under Assumption 2, for any morphology $i \in \mathcal{M}$,

$$R_i(\theta^+) \leq R_i(\theta) - \eta \left(w_i \|g_i(\theta)\|^2 + \sum_{j \neq i} w_j \langle g_i(\theta), g_j(\theta) \rangle \right) + \frac{L\eta^2}{2} \left\| \sum_{j=1}^K w_j g_j(\theta) \right\|^2. \quad (14)$$

Proof of Theorem 1. Fix an arbitrary morphology $i \in \mathcal{M}$. We apply the L -smoothness inequality (Assumption 2) to the function R_i , with the pair $(\theta, \theta') = (\theta, \theta^+)$. By definition of the shared update, we have

$$\theta^+ - \theta = -\eta \sum_{j=1}^K w_j g_j(\theta).$$

Substituting $\theta' = \theta^+$ and $\theta' - \theta = \theta^+ - \theta$ into the smoothness inequality yields

$$R_i(\theta^+) \leq R_i(\theta) + \langle g_i(\theta), \theta^+ - \theta \rangle + \frac{L}{2} \|\theta^+ - \theta\|^2. \quad (15)$$

Using $\theta^+ - \theta = -\eta \sum_{j=1}^K w_j g_j(\theta)$, the inner product in Eq. (15) becomes

$$\begin{aligned} \langle g_i(\theta), \theta^+ - \theta \rangle &= \left\langle g_i(\theta), -\eta \sum_{j=1}^K w_j g_j(\theta) \right\rangle \\ &= -\eta \sum_{j=1}^K w_j \langle g_i(\theta), g_j(\theta) \rangle. \end{aligned} \quad (16)$$

Now separate the $j = i$ term from the rest:

$$\begin{aligned} \sum_{j=1}^K w_j \langle g_i(\theta), g_j(\theta) \rangle &= w_i \langle g_i(\theta), g_i(\theta) \rangle + \sum_{j \neq i} w_j \langle g_i(\theta), g_j(\theta) \rangle \\ &= w_i \|g_i(\theta)\|^2 + \sum_{j \neq i} w_j \langle g_i(\theta), g_j(\theta) \rangle. \end{aligned} \quad (17)$$

Combining Eq. (16) and Eq. (17), we obtain

$$\langle g_i(\theta), \theta^+ - \theta \rangle = -\eta \left(w_i \|g_i(\theta)\|^2 + \sum_{j \neq i} w_j \langle g_i(\theta), g_j(\theta) \rangle \right). \quad (18)$$

Again using $\theta^+ - \theta = -\eta \sum_{j=1}^K w_j g_j(\theta)$, we have

$$\|\theta^+ - \theta\|^2 = \left\| -\eta \sum_{j=1}^K w_j g_j(\theta) \right\|^2 = \eta^2 \left\| \sum_{j=1}^K w_j g_j(\theta) \right\|^2. \quad (19)$$

Therefore,

$$\frac{L}{2} \|\theta^+ - \theta\|^2 = \frac{L\eta^2}{2} \left\| \sum_{j=1}^K w_j g_j(\theta) \right\|^2. \quad (20)$$

Substituting Eq. (18) and Eq. (20) into Eq. (15), we conclude

$$R_i(\theta^+) \leq R_i(\theta) - \eta \left(w_i \|g_i(\theta)\|^2 + \sum_{j \neq i} w_j \langle g_i(\theta), g_j(\theta) \rangle \right) + \frac{L\eta^2}{2} \left\| \sum_{j=1}^K w_j g_j(\theta) \right\|^2,$$

which is exactly Eq. (14). This completes the proof. \square

Remark 3 (Connection to isolation and gradient interference). Equation (14) decomposes the change of R_i into a beneficial self term and certain cross terms. Specifically, the self term is defined as $w_i \|g_i(\theta)\|^2$ while the cross terms are expressed as the inner product $\langle g_i(\theta), g_j(\theta) \rangle$. These cross terms quantify the extent to which updates favored by other morphologies influence task i . When these terms remain persistently negative throughout the training process, the shared update contains a nontrivial component pointing against the descent direction of R_i . This conflict reduces the effective descent and may stall or even increase R_i depending on the respective magnitudes of the terms. This phenomenon represents the core mechanism of gradient interference within shared parameters. Isolation training removes these cross terms by construction because each expert is optimized using only its own gradient. Consequently, this approach eliminates the dominant source of interference before the reconciliation or merging phases.

A.3 Spatial Scaffold as a Universal Bridge: A Transfer Bound

This subsection formalizes the universal bridge claim of spatial intelligence by deriving a transfer bound from spatial-scaffold training to an unseen target morphology. The result shows that the target risk is controlled by the recoverability of the shared geometric scaffold and the geometric mismatch between the target morphology and the scaffold training distribution, thereby providing a theoretical justification for the effectiveness of the SCAFFOLD stage.

Assumption 3 (Lipschitz Dependence on Geometry). *There exists $L_g > 0$ such that for any c and any $g, g' \in \mathcal{G}$,*

$$|\ell(g, c; \theta) - \ell(g', c; \theta)| \leq L_g \|g - g'\|,$$

where $\ell(g, c; \theta)$ denotes the loss evaluated on samples whose semantics are governed by g .

Assumption 3 is grounded in the inherent continuity of spatial supervision signals such as distance, orientation, and temporal metrics. This smoothness persists near reachability boundaries where minor geometric deviations produce bounded loss variations. A Lipschitz condition formally encapsulates this stability property. Furthermore such regularity assumptions represent standard theoretical frameworks extensively utilized in machine learning [131, 132].

Assumption 4 (Geometric Distribution Shift). *Let $P_G^{(m)}$ be the marginal distribution of g induced by D_m . Let $P_G^{(\text{sp})}$ be the geometric marginal induced by the spatial scaffold distribution. Assume there exists a discrepancy measure $\text{Disc}(\cdot, \cdot)$ and a constant $\delta_m \geq 0$ such that*

$$\text{Disc}(P_G^{(m)}, P_G^{(\text{sp})}) \leq \delta_m.$$

Assumption 4 represents morphological diversity as an interpretable scalar δ_m using a geometric discrepancy bound. This formulation simplifies complex distributional shifts by assuming a valid measure exists to satisfy $\text{Disc}(P_G^{(m)}, P_G^{(\text{sp})}) \leq \delta_m$. Theoretically, δ_m quantifies the transfer impact of geometric mismatches which is supported by the observed performance asymmetries across different viewpoints and motion patterns. Practical success in broadening the scaffold distribution further confirms that reducing this discrepancy directly enhances cross embodiment generalization. This strategy aligns with standard transfer learning theories where a discrepancy metric bounds the shift between source and target domains [133].

Theorem 2 (Scaffold-to-morphology transfer bound). *Assume Assumptions 1–4. Let θ_{spatial} be obtained from scaffold spatial training. Then for any target morphology $m \in \mathcal{M}$,*

$$R_m(\theta_{\text{spatial}}) \leq R_{\text{sp}}(\theta_{\text{spatial}}) + C_m \delta_m + 2L_g \varepsilon_g + \varepsilon_m, \quad (21)$$

where $R_{\text{sp}}(\theta)$ is the risk under the scaffold distribution, C_m can be taken as a constant proportional to L_g , δ_m quantifies geometric shift, and ε_m aggregates residual morphology-dependent effects.

Proof of Theorem 2. Fix a target morphology $m \in \mathcal{M}$ and consider $\theta = \theta_{\text{spatial}}$. We prove Eq. (21) by decomposing the target risk into: (i) a scaffold risk term, (ii) a representation-to-geometry recovery error term, and (iii) a geometric marginal shift term, plus residual morphology-dependent effects.

From shared geometric scaffold mechanism, we have $o = \Psi_m(g, a_m)$ and $y = \Phi(g, c)$. Let the learning system incur a per-sample loss $\ell_\theta(o, c, y)$. Define the target risk

$$R_m(\theta) = \mathbb{E}_{(o,c,y) \sim D_m} [\ell_\theta(o, c, y)],$$

and similarly define $R_{\text{sp}}(\theta)$ under the scaffold (spatial) distribution.

Then, conditional on (g, c) , the semantics of y is approximately morphology-invariant and most morphology-dependence is absorbed by the observation channel. Formally, we introduce an ideal semantic loss $\ell(g, c; \theta)$ such that

$$\left| \mathbb{E} [\ell_\theta(o, c, y) \mid g, c] - \ell(g, c; \theta) \right| \leq \Delta_m(g, c; \theta), \quad (22)$$

where Δ_m quantifies the residual dependence on morphology-specific factors (e.g., imperfect invariance, weak dependence on a_m , or dependence on the observation channel not fully mediated by g). Define the aggregated residual term

$$\varepsilon_m := \mathbb{E}_{(g,c) \sim P_{G,C}^{(m)}} [\Delta_m(g, c; \theta_{\text{spatial}})],$$

which is finite by construction.

Taking expectation of Eq. (22) over (g, c) induced by D_m , we obtain

$$\begin{aligned} R_m(\theta_{\text{spatial}}) &= \mathbb{E}_{(g,c) \sim P_{G,C}^{(m)}} [\mathbb{E}[\ell_{\theta_{\text{spatial}}}(o, c, y) \mid g, c]] \\ &\leq \mathbb{E}_{(g,c) \sim P_{G,C}^{(m)}} [\ell(g, c; \theta_{\text{spatial}})] + \varepsilon_m. \end{aligned} \quad (23)$$

Thus it suffices to upper-bound the semantic risk under the target geometry distribution.

Let $\hat{g} := \text{Dec}(h_{\theta_{\text{spatial}}}(o, c))$ be the recovered geometry from the learned representation. By Assumption 3, for any (g, c) ,

$$|\ell(g, c; \theta_{\text{spatial}}) - \ell(\hat{g}, c; \theta_{\text{spatial}})| \leq L_g \|g - \hat{g}\|. \quad (24)$$

Taking expectation over (o, c) drawn from the scaffold (spatial) distribution and using Assumption 1, we get

$$\begin{aligned} \mathbb{E}_{\text{sp}} [|\ell(g, C; \theta_{\text{spatial}}) - \ell(\hat{g}, C; \theta_{\text{spatial}})|] &\leq L_g \mathbb{E}_{\text{sp}} [\|g - \hat{g}\|] \\ &\leq L_g \varepsilon_g. \end{aligned} \quad (25)$$

To relate the target semantic expectation $\mathbb{E}_{(g,c) \sim P_{G,C}^{(m)}} [\ell(g, c; \theta_{\text{spatial}})]$ to scaffold quantities, we add and subtract the recovered-geometry loss and use triangle inequality:

$$\mathbb{E}_{(g,c) \sim P_{G,C}^{(m)}} [\ell(g, c; \theta_{\text{spatial}})] \leq \mathbb{E}_{(g,c) \sim P_{G,C}^{(m)}} [\ell(\hat{g}, c; \theta_{\text{spatial}})] + \mathbb{E}_{(g,c) \sim P_{G,C}^{(m)}} [|\ell(g, c; \theta_{\text{spatial}}) - \ell(\hat{g}, c; \theta_{\text{spatial}})|]. \quad (26)$$

The second term is a geometry-recovery error term under target distribution. Then, we upper-bound it by a constant times ε_g and absorb any target-vs-scaffold mismatch into the constant. Concretely, there exists a constant $C_m^{(1)}$ proportional to L_g such that

$$\mathbb{E}_{(g,C) \sim P_{G,C}^{(m)}} [|\ell(g, C; \theta_{\text{spatial}}) - \ell(\hat{g}, C; \theta_{\text{spatial}})|] \leq C_m^{(1)} \varepsilon_g. \quad (27)$$

It remains to relate $\mathbb{E}_{(g,c) \sim P_{G,C}^{(m)}} [\ell(\hat{g}, c; \theta_{\text{spatial}})]$ to the corresponding expectation under the scaffold distribution. Let \mathcal{F}_m denote the function class induced by the learned system at θ_{spatial} . By Assumption 4, we have

$$\text{Disc}(P_G^{(m)}, P_G^{(\text{sp})}) \leq \delta_m.$$

By the defining property of Disc as an IPM-like discrepancy over \mathcal{F}_m , there exists a constant $C_m^{(2)}$ such that

$$\left| \mathbb{E}_{g \sim P_G^{(m)}} [f(g)] - \mathbb{E}_{g \sim P_G^{(\text{sp})}} [f(g)] \right| \leq C_m^{(2)} \delta_m, \quad \forall f \in \mathcal{F}_m. \quad (28)$$

Applying Eq. (28) to the particular f induced by $\ell(\cdot, \cdot; \theta_{\text{spatial}})$ yields

$$\mathbb{E}_{(g,c) \sim P_{G,C}^{(m)}}[\ell(g, c; \theta_{\text{spatial}})] \leq \mathbb{E}_{(g,c) \sim P_{G,C}^{(\text{sp})}}[\ell(g, c; \theta_{\text{spatial}})] + C_m^{(2)} \delta_m. \quad (29)$$

Under the scaffold distribution, the semantic loss upper-bounds the realized loss: by reversing the construction in Eq. (22) for the scaffold domain and absorbing the corresponding residual into constants, we can write

$$|R_{\text{sp}}(\theta_{\text{spatial}}) - \mathbb{E}_{(g,c) \sim P_{G,C}^{(\text{sp})}}[\ell(g, c; \theta_{\text{spatial}})]| \leq \varepsilon_{\text{sp}}, \quad (30)$$

where ε_{sp} is a typically small approximation term for the scaffold domain. Since the theorem statement allows an aggregate residual term for morphology-dependent effects, we absorb ε_{sp} into ε_m without loss of generality.

From Eq. (23) and Eq. (29),

$$R_m(\theta_{\text{spatial}}) \leq \mathbb{E}_m[\ell(g, C; \theta_{\text{spatial}})] + \varepsilon_m \quad (31)$$

$$\leq \mathbb{E}_{\text{sp}}[\ell(g, C; \theta_{\text{spatial}})] + C_m^{(2)} \delta_m + \varepsilon_m. \quad (32)$$

Now add and subtract $\ell(\hat{g}, C; \theta_{\text{spatial}})$ under the scaffold distribution:

$$\mathbb{E}_{\text{sp}}[\ell(g, C; \theta_{\text{spatial}})] \leq \mathbb{E}_{\text{sp}}[\ell(\hat{g}, C; \theta_{\text{spatial}})] + \mathbb{E}_{\text{sp}}[|\ell(g, C; \theta_{\text{spatial}}) - \ell(\hat{g}, C; \theta_{\text{spatial}})|] \quad (33)$$

$$\leq \mathbb{E}_{\text{sp}}[\ell(\hat{g}, C; \theta_{\text{spatial}})] + L_g \mathbb{E}_{\text{sp}}\|g - \hat{g}\| \leq \mathbb{E}_{\text{sp}}[\ell(\hat{g}, C; \theta_{\text{spatial}})] + L_g \varepsilon_g, \quad (34)$$

where we used Assumptions 3 and 1. Finally, relate $\mathbb{E}_{\text{sp}}[\ell(\hat{g}, C; \theta_{\text{spatial}})]$ back to R_{sp} : by Eq. (30) and the same Lipschitz-recoverability step,

$$\mathbb{E}_{\text{sp}}[\ell(\hat{g}, C; \theta_{\text{spatial}})] \leq \mathbb{E}_{\text{sp}}[\ell(g, C; \theta_{\text{spatial}})] + L_g \varepsilon_g \leq R_{\text{sp}}(\theta_{\text{spatial}}) + \varepsilon_{\text{sp}} + L_g \varepsilon_g. \quad (35)$$

Combining the above yields

$$R_m(\theta_{\text{spatial}}) \leq R_{\text{sp}}(\theta_{\text{spatial}}) + C_m^{(2)} \delta_m + 2L_g \varepsilon_g + (\varepsilon_m + \varepsilon_{\text{sp}}).$$

Absorb constants into C_m and absorb ε_{sp} into ε_m to obtain Eq. (21). This completes the proof. \square

Remark 4 (What the bound captures and its experimental implications). *Eq. (21) decomposes the target-morphology risk after the SCAFFOLD stage into a recoverability term, a geometric-shift term, and a morphology-specific residual. The term $L_g \varepsilon_g$ isolates the effect of geometric recoverability: as spatial training reduces the decoding error ε_g of the shared scaffold g , the target risk decreases proportionally to the sensitivity constant L_g . This provides a direct theoretical explanation for the empirical trend that stronger geometry-aware pretraining signals and improved 3D supervision yield systematic gains in zero-shot transfer across diverse embodiments.*

The term $C_m \delta_m$ characterizes transfer sensitivity to geometric distribution mismatch between the target morphology and the scaffold training distribution. For a fixed ε_g , differences in δ_m induce cross-embodiment performance asymmetries, predicting strong transfer under shared spatial regimes and degraded transfer when the target exhibits substantially different viewpoints, motion patterns, scale statistics, or scene topology. This aligns with the observed improvement from broadening the scaffold distribution, which effectively reduces δ_m .

The residual ε_m aggregates factors not fully mediated by geometry, including embodiment-specific sensing artifacts, dynamics constraints, actuation semantics, and output-space idiosyncrasies. It explains why spatial scaffold pretraining can deliver substantial gains yet typically does not close the gap to morphology-specialized training, and it clarifies that the subsequent RECONCILE stage primarily targets this remaining morphology-dependent component rather than relearning the shared spatial core.

A.4 Visualization on Spatial Benchmarks

In this section, we present qualitative visualizations on spatial benchmarks to illustrate the spatial cognition of ACE-Brain-0. Specifically, we include examples from six representative spatial benchmarks: VSI [82] (Fig. 5, 6, 7, 8, and 9), MMSI [83] (Fig. 10), BLINK [84] (Fig. 11), SAT [67] (Fig. 12 and 13), SITE (Fig. 14 and 15), and MindCube [68] (Fig. 16, 17, and 18).

Specifically, for examples 1-4 of VSI shown in Fig. 5, 6, 7, and 8, ACE-Brain-0 successfully predicts the room area (32.4 m²), selects the correct navigation path (“Turn Left, Turn Right”), accurately estimates the distance between the washer and the toilet (0.8 m), and measures the longest dimension of the lamp (184 cm), jointly demonstrating its capability for scale-aware metric estimation and consistent multi-view 3D spatial reasoning across diverse indoor scenarios. However, in Example 5, the model predicts 2 suitcases instead of the ground-truth 3, which likely stems from the ambiguous everyday definition of the blue object, an item that can reasonably be interpreted as either a suitcase or a backpack, showing the vague categorization rather than limitation in spatial comprehension.

For Examples 1 and 2 of MMSI shown in Fig. 10, ACE-Brain-0 correctly infers that the dining table is located to the southwest of the stairs in Example 1, demonstrating object-to-object directional comprehension. However, in Example 2, it predicts “front right” instead of the ground-truth “front left”, suggesting that viewpoint transformation remains challenging in complex indoor layouts.

For Examples 1-4 of BLINK shown in Fig. 11, ACE-Brain-0 correctly identifies closer objects from monocular depth cues, resolves cross-scene spatial relations, verifies object presence under partial occlusion, and determines whether the dog is on the motorcycle, jointly demonstrating its capability for relative depth estimation, and visually grounded verification in diverse real-world scenarios.

For examples 1 and 2 of SAT shown in Fig. 12, ACE-Brain-0 correctly detects object displacement across frames, identifying that the chair moves left and away from the camera and that the bottle moves left and towards the camera, demonstrating its capability for temporal spatial observations. For Examples 3 and 4 of SAT shown in Fig. 13, ACE-Brain-0 correctly infers the rotation of viewpoint, demonstrating its capability for camera motion understanding.

For examples 1 and 2 of SITE shown in Fig. 14 and 15, ACE-Brain-0 correctly selects the images that match the given spatial descriptions (“bed in the bottom-left corner” and “motorbike at the top-right”), demonstrating its capability for understanding visual layouts between multiple misleading samples.

For examples 1–3 of MindCube shown in Fig. 16, 17, and 18, ACE-Brain-0 correctly infers that the large recycling bin is behind the small one from a different viewpoint, predicts that turning right and moving forward would increase the distance to the vending machine, and identifies the white table as the nearest object to the left when repositioned at the sofa’s location, jointly demonstrating its capability for relative size understanding, occlusion-aware spatial observation, and viewpoint-consistent comprehension.

A.5 Visualization on AD Benchmarks

In this section, we present qualitative visualizations on autonomous driving benchmarks to illustrate the driving-related perception and reasoning capabilities of ACE-Brain-0. Specifically, we include examples from four representative benchmarks: NuscenesQA [92] (Fig. 19, 20, and 21), NuPlanQA [70] (Fig. 22), MAPLM [90], and LingoQA [93], covering multi-view scene understanding, dynamic object reasoning, planning-aware comprehension, and language-grounded driving semantics.

Specifically, for examples 1-3 of NuscenesQA shown in Fig. 19, 20, and 21, ACE-Brain-0 correctly identifies that no moving bicycles are visible, localizes the pedestrian positioned at the back-right of the bus, and counts 10 objects sharing the same status as the truck across multiple views. These examples demonstrate its capability for cross-view dynamic object recognition, spatially constrained localization, and counting in complex urban driving scenarios.

For example 1 of NuPlanQA shown in Fig. 22, ACE-Brain-0 correctly identifies that a red traffic light is visible ahead by integrating multi-view scene observations with temporal vehicle state signals (velocity and

steering angles over the past 1.5 seconds). This example illustrates its capability for kinematics understanding, and traffic signal perception in complex urban scenes.

For examples 1 and 2 of MAPLM shown in Fig. 23 and 24, ACE-Brain-0 correctly classifies the road scenes as a normal city road and an undeveloped road, respectively, by integrating LiDAR bird’s-eye-view representations with multi-view images. These examples illustrate its capability for cross-modal scene understanding, road-type discrimination, and robust environmental interpretation under varying lighting and conditions in autonomous driving scenarios.

For examples 1 and 2 of LingoQA shown in Fig. 25 and 26, ACE-Brain-0 correctly identifies a temporary traffic light displaying green across temporal frames and infers that the ego-vehicle is accelerating. However, although the output in example 2 is correct, the generated justification does not fully capture the most critical dynamic factor that the leading truck is moving off, indicating that while the model understands the scene, its explanation generation could benefit from stronger alignment with causal reasoning data. These examples illustrate ACE-Brain-0’s capability for temporal traffic signal recognition, causal scene interpretation, and basic justification for explainable autonomous driving decision understanding.

A.6 Visualization on UAV Benchmarks

In this section, we present qualitative visualizations on low-altitude UAV benchmarks to illustrate the aerial perception and spatial reasoning capability of ACE-Brain-0. Specifically, we include examples from three representative benchmarks: UrbanVideo-Bench [11] (Fig. 27), AirCopBench [8] (Fig. 28 and 29), and AVI-Math [59] (Fig. 30 and 31).

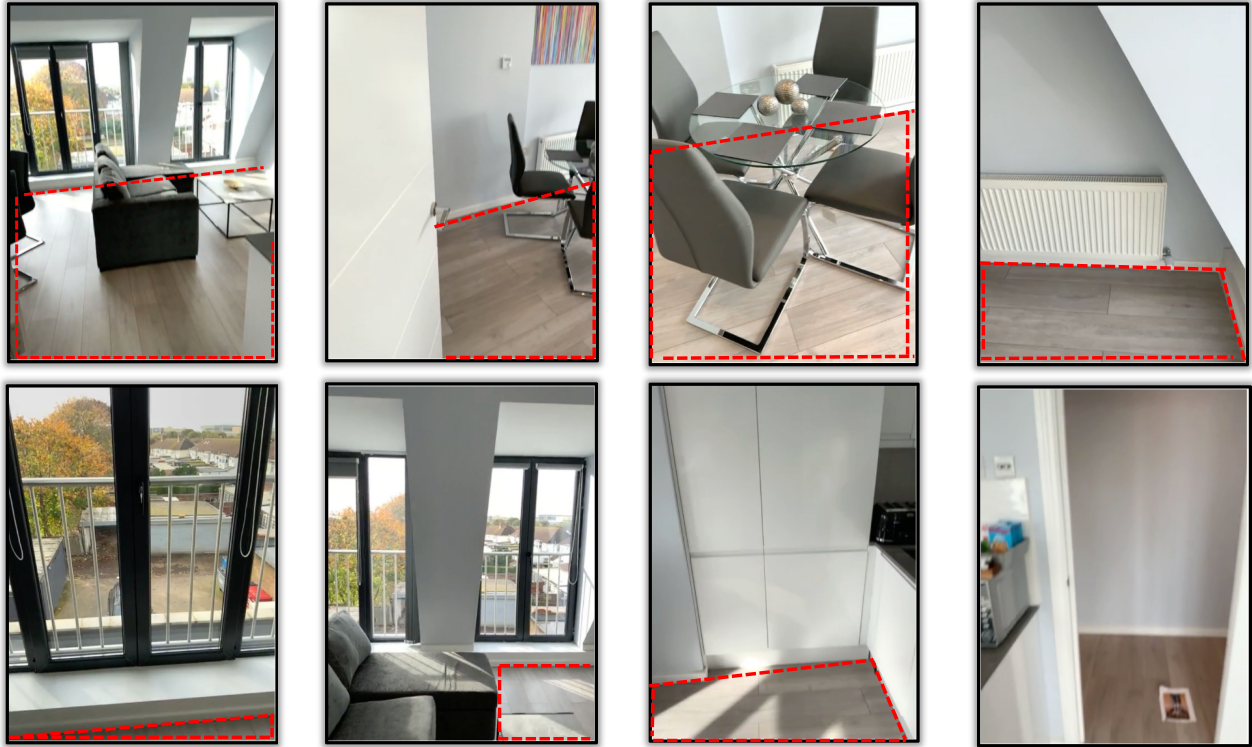
For examples 1 and 2 of UrbanVideo-Bench shown in Fig. 27, ACE-Brain-0 correctly reconstructs the upward-then-horizontal flight trajectory toward the largest nearby intersection and identifies the biggest crossroads within the field of view at the current location. These examples demonstrate its capability for large-scale landmark recognition, and viewpoint-consistent spatial comprehension from multi-frame drone observations.

For examples 1 and 2 of AirCopBench shown in Fig. 28, ACE-Brain-0 correctly determines that the white van is in the same lane as the white truck but ahead of it, and identifies the white car approaching the intersection from the bottom as the vehicle directly opposite the yellow bus. For examples 3 and 4 of AirCopBench shown in Fig. 29, ACE-Brain-0 correctly infers that there are no pedestrians on the zebra crossing and identifies the red car as being in a parallel lane to the white van. These examples illustrate its capability for aerial intersection monitoring, traffic participant interaction analysis, and lane-level relational reasoning in complex urban road topologies.

For Examples 1–4 of AVI-Math shown in Fig. 30, ACE-Brain-0 correctly confirms the presence of Monica’s car and identifies two vehicles requiring regular refueling, while more notably, in Examples 3 and 4, it predicts the center coordinates of the vehicle within a specified ground-plane camera coordinate system. In Example 3, it accurately outputs the correct coordinate $([-23, -7, 49])$, and in Example 4, although the predicted value $([0, 9.54, 30.28])$ is not exactly identical to the ground truth $([0, 9, 32])$, it remains geometrically consistent under large-resolution (4000×2250) aerial images. These examples highlight its capability for structured numerical reasoning under explicit coordinate systems, geometry-aware point localization, and complex spatial computation from aerial viewpoints. For Examples 5–7 of AVI-Math shown in Fig. 31, ACE-Brain-0 correctly estimates the drone’s altitude (30 m) and reasonably approximates the time required to reach the closest vehicle based on the given flight speed, while also predicting pixel-level coordinates of a specified 3D projection point. Although the predicted image coordinates are not exactly identical to the ground truth, they remain close in magnitude and direction, reflecting geometrically coherent reasoning under the defined camera model. These examples further demonstrate its capability for metric estimation, coordinate transformation, and geometry-aware understanding from aerial imagery.

A.7 Visualization on Embodied Benchmarks

In this section, we present qualitative visualizations on embodied benchmarks to illustrate the embodied perception, action prediction, and interaction understanding capabilities of ACE-Brain-0. We include examples



Question: What is the size of this room (in square meters)?
 If multiple rooms are shown, estimate the size of the combined space.
Ground-Truth: 30.9
ACE-Brain Output: 32.4

Figure 5 Example 1 of VSI Benchmark.

from three representative benchmarks: RoboVQA [96] (Fig. 32, 33, and 34), OpenEQA [97] (Fig. 35 and 36), and EgoPlan-Bench2 [99] (Fig. 37 and 38), covering egocentric manipulation understanding, embodied question answering, and goal-oriented planning in interactive environments.

For examples 1–3 of RoboVQA shown in Fig. 32, 33, and 34, ACE-Brain-0 correctly infers that the orange is placed into the bowl, recognizes that the feasible next action involves moving the chair away from the table (despite generating a more general description “adjust the chair”), and identifies that the pen is placed into the stand. These examples demonstrate its capability for temporal action understanding, object affordance recognition, and fine-grained manipulation reasoning from egocentric visual sequences in embodied scenarios.

For examples 1 and 2 of OpenEQA shown in Fig. 35 and 36, ACE-Brain-0 correctly identifies the bedroom as the room containing the car by integrating multi-view indoor observations, and infers that cotton swabs are most likely stored in the sink cabinet within the bathroom. These examples illustrate its capability for room-level localization, indoor topology understanding, and commonsense reasoning about object-function associations in embodied navigation scenarios.

For examples 1 and 2 of EgoPlan-Bench2 shown in Fig. 37 and 38, ACE-Brain-0 correctly infers the next required action by integrating prior video progress with the current egocentric observation, identifying “turn off sink tap” in the kitchen scenario and “pick water bottle” in the rowing scenario. These examples demonstrate its capability for long-horizon procedural reasoning, temporal context integration, and goal-directed action prediction in dynamic embodied tasks.



Question: You are a robot **beginning at the door and facing the standing lamps**. You want to **navigate to the tv**. You will perform the following actions (Note: for each [please fill in], choose either 'turn back,' 'turn left,' or 'turn right.'): 1. Go forward until the **sofa**. 2. [please fill in] 3. Go forward until the **fireplace**. 4. [please fill in] 5. Go forward until the **tv**. You have reached the final destination.

Options:

- A. Turn Back, Turn Left B. Turn Right, Turn Left
- C. Turn Left, Turn Left D. Turn Left, Turn Right

Ground-Truth: D. Turn Left, Turn Right

ACE-Brain Output: D. Turn Left, Turn Right

Figure 6 Example 2 of VSI Benchmark.

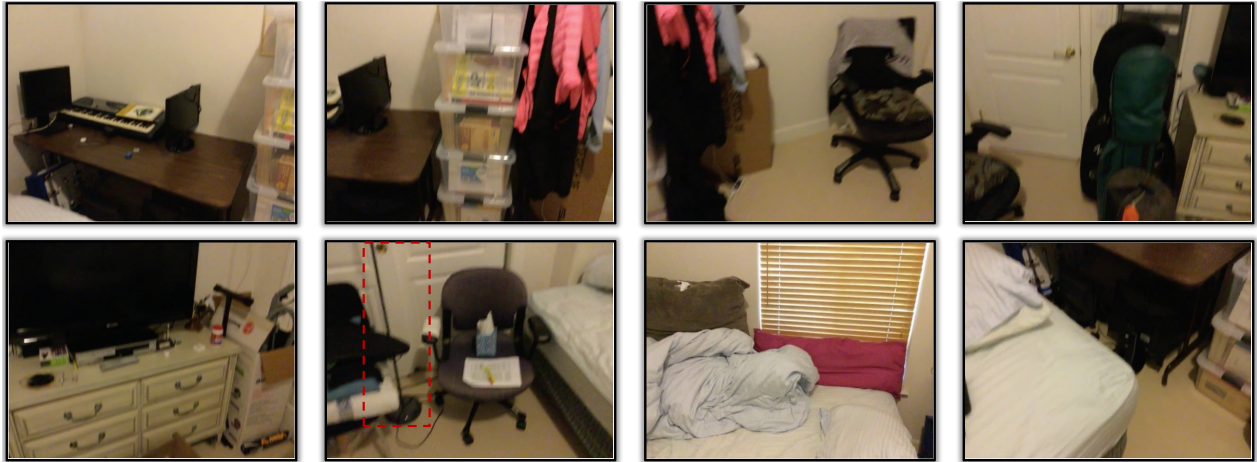


Question: Measuring from the **closest point** of each object, what is the **distance** between the **washer** and the **toilet** (in meters)?

Ground-Truth: 0.8

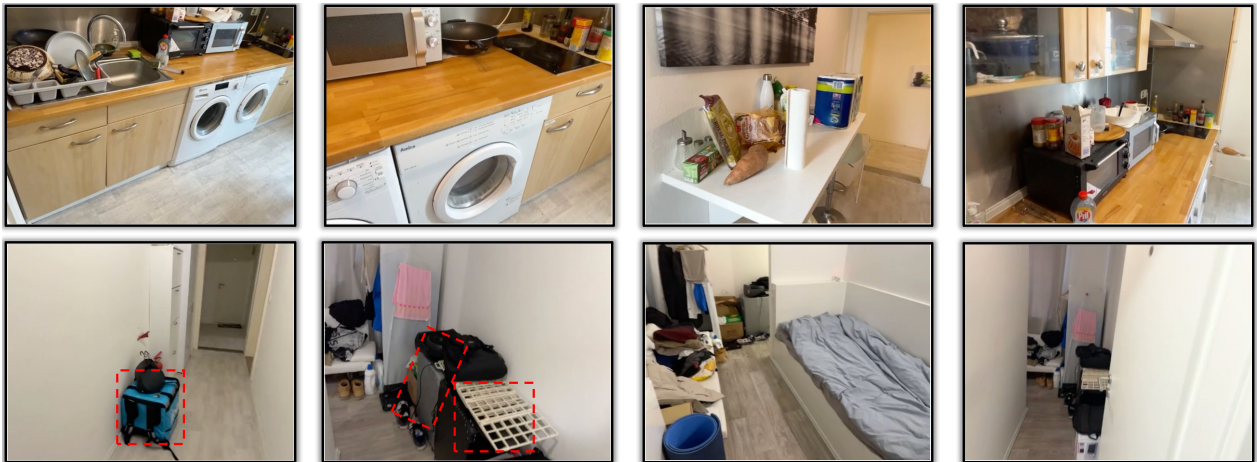
ACE-Brain Output: 0.8

Figure 7 Example 3 of VSI Benchmark.



Question: What is the length of the longest dimension (length, width, or height) of the lamp, measured in centimeters?
Ground-Truth: 179
ACE-Brain Output: 184

Figure 8 Example 4 of VSI Benchmark.



Question: How many suitcase(s) are in this room?
Ground-Truth: 3
ACE-Brain Output: 2

Figure 9 Example 5 of VSI Benchmark.

Question: The display cabinet is on the east side of the living room. In which direction from the stairs is the dining table located?

Options:
A. Northeast B. Northwest C. Southeast D. Southwest

Ground-Truth: D. Southwest
ACE-Brain Output: D. Southwest

Question: May I ask, when you are sitting on the chair next to the plant, where is the desk lamp located relative to you?

Options:
A. Front left B. Directly in front
C. Front right D. Directly to the left

Ground-Truth: A. Front left
ACE-Brain Output: C. Front right

Figure 10 Example 1-2 of MMSI Benchmark.

Question: Which point is closer to the camera?

Options: A. A is closer B. B is closer

Ground-Truth: B
ACE-Brain Output: B

Question: Which point is closer to the camera?

Options: A. A is closer B. B is closer

Ground-Truth: A
ACE-Brain Output: A

Question: Is the person left of the refrigerator?

Options: A.yes B.no

Ground-Truth: A
ACE-Brain Output: A

Question: Is the dog on the motorcycle?

Options: A.yes B.no

Ground-Truth: B
ACE-Brain Output: B

Figure 11 Example 1-4 of BLINK Benchmark.

Question: Were any of the objects in the initial frame that you can still see in the second frame moved from their original positions?

Options:
A. chair was moved left and away from the camera
B. chair was moved right and away from the camera

Ground-Truth: A. chair was moved left and away from the camera
ACE-Brain Output: A. chair was moved left and away from the camera

Question: Were any of the objects in the initial frame that you can still see in the second frame moved from their original positions?

Options:
A. bottle was moved left and towards the camera
B. bottle was moved right and towards the camera

Ground-Truth: A. bottle was moved left and towards the camera
ACE-Brain Output: A. bottle was moved left and towards the camera

Figure 12 Example 1-2 of SAT Benchmark.



Question: How did the camera likely rotate when shooting the video?

Options: A. rotated left B. rotated right

Ground-Truth: A. rotated left

ACE-Brain Output: A. rotated left

Question: How did the camera likely rotate when shooting the video?

Options: A. rotated right B. rotated left

Ground-Truth: A. rotated right

ACE-Brain Output: A. rotated right

Figure 13 Example 3-4 of SAT Benchmark.

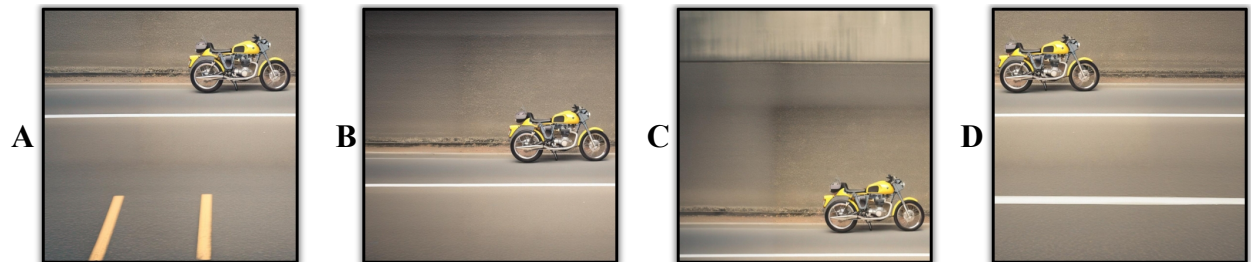


Question: The bed is in the bottom-left corner of the image. Please choose the best image that matches the description.

Ground-Truth: B

ACE-Brain Output: B

Figure 14 Example 1 of SITE Benchmark.



Question: The motorbike is at the top-right of the image. Please choose the best image that matches the description.

Ground-Truth: A

ACE-Brain Output: A

Figure 15 Example 2 of SITE Benchmark.



Question: Based on these three images (image 1, 2, and 3) showing the same scene from different viewpoints (back, left, and right): From the viewpoint presented in image 2, is there a **large blue recycling bin behind the small blue recycling bin**?

Options: A. No B. Yes

Ground-Truth: B. Yes

ACE-Brain Output: B. Yes

Figure 16 Example 1 of MindCube Benchmark.



Question: Based on these three images (image 1, 2, and 3) showing the same scene from different viewpoints (front, left, and right): If I am standing at the same spot and facing the same direction as shown in **image 2**, then I **turn right and move forward**, what **would happen** to my relative position to the **blue vending machine**?

Options:

A. It would become closer to me. B. The distance wouldn't change much, but it would be on my front-left.

C. The distance wouldn't change much, but it would be on my front-right. D. It would become farther from me.

Ground-Truth: D. It would become farther from me.

ACE-Brain Output: D. It would become farther from me.

Figure 17 Example 2 of MindCube Benchmark.



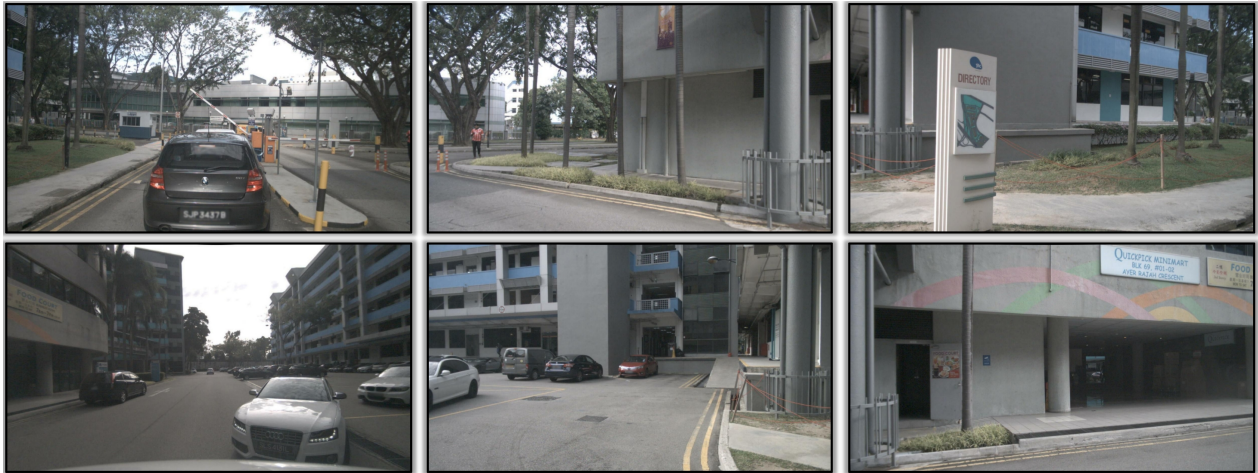
Question: Based on these three images (image 1, 2, and 3) showing the same scene from different viewpoints (front, left, and right): In image 2, if I was positioned where the **sofa** is, **facing the same direction as it**, what would be the **nearest object to my left**?

Options: A. White table B. Grey bin C. Blue bin

Ground-Truth: A. White table

ACE-Brain Output: A. White table

Figure 18 Example 3 of MindCube Benchmark.

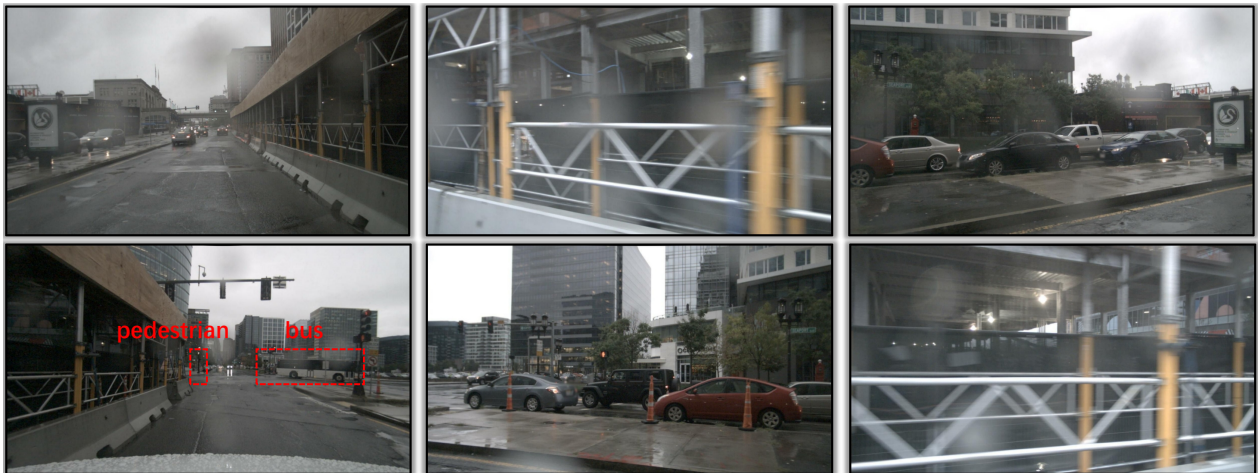


Question: Are any moving bicycles visible?

Ground-Truth: no

ACE-Brain Output: no

Figure 19 Example 1 of NuscenesQA Benchmark.



Question: The moving thing that is to the back right of the bus is what?

Ground-Truth: pedestrian

ACE-Brain Output: pedestrian

Figure 20 Example 2 of NuscenesQA Benchmark.

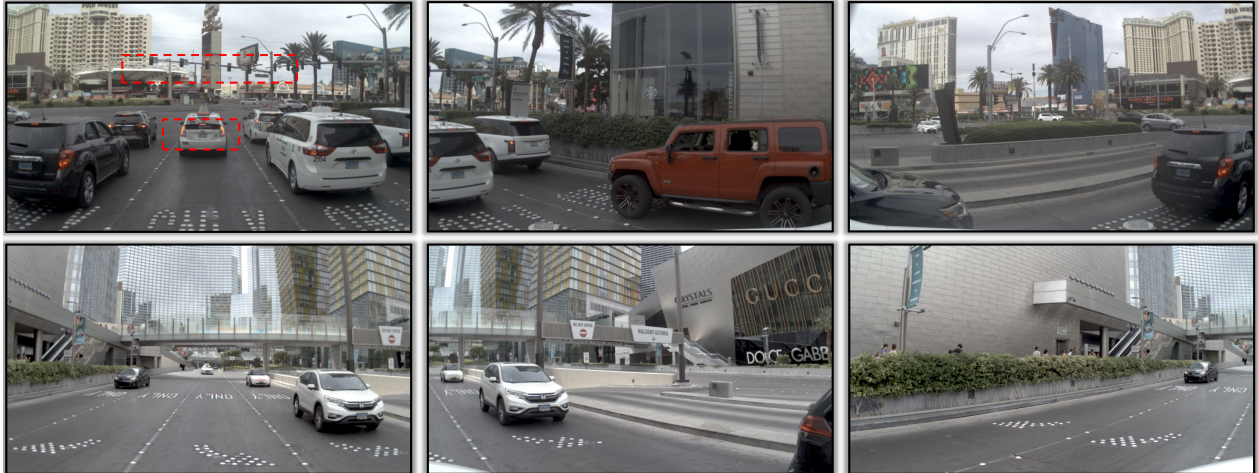


Question: What number of other things are in the **same status** as the **truck**?

Ground-Truth: 10

ACE-Brain Output: 10

Figure 21 Example 3 of NuscenesQA Benchmark.



You are driving on the road. Based on given images of the surroundings of your vehicle and information from your vehicle extracted **past 1.5 seconds**, choose right answer among (a) to (d) for the given question.

- **Velocity(m/s):** [5.324, 4.671, 4.045, 3.469, 2.84]

- **Steering angles:** [-0.027, -0.008, 0.171, 0.424, 0.236]

Question: Are there any **traffic lights** ahead that the ego-vehicle must follow?

Options: A. Red light is visible B. Yellow light is visible C. Green light is visible D. No traffic light is visible

Ground-Truth: A. Red light is visible

ACE-Brain Output: A. Red light is visible

Figure 22 Example 1 of NuPlanQA Benchmark.



Question: What kind of road scene is it in the images?
Options: A. Normal city road. B. Construction road. C. Undeveloped road. D. Road mark repainting.
 E. Roundabout. F. None of the above.
Ground-Truth: A. Normal city road.
ACE-Brain Output: A. Normal city road.

Figure 23 Example 1 of MAPLM Benchmark.



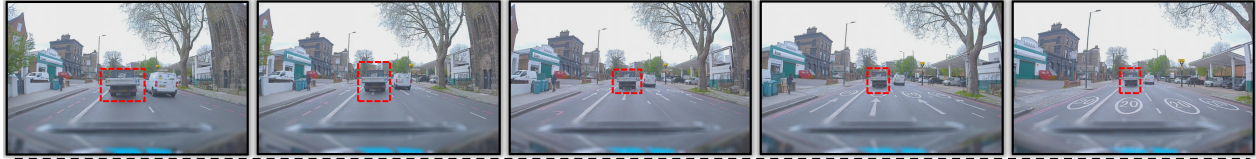
Question: What kind of road scene is it in the images?
Options: A. Normal city road B. Construction road C. Undeveloped road D. Road mark repainting
 E. Roundabout F. None of the above
Ground-Truth: C. Undeveloped road
ACE-Brain Output: C. Undeveloped road

Figure 24 Example 2 of MAPLM Benchmark.



Question: Is there a traffic light? If yes, what color is displayed?
Ground-Truth: Yes, a temporary traffic light. It is showing green.
ACE-Brain Output: Yes, there are traffic lights and they are showing green.

Figure 25 Example 1 of LingoQA Benchmark.



Question: What is the **current action** and its **justification**? Answer in the form 'action, justification'.

Ground-Truth: The car accelerates, as the truck in front in its lane is moving off.

ACE-Brain Output: **Accelerating**, because **there is a gap in the traffic behind the truck ahead.**

Figure 26 Example 2 of LingoQA Benchmark.



Question: You are navigating to the **largest nearby intersection**. What is the correct summary of your trajectory **from the start to the current location**?

Options:

- A. Start from the parking lot, drive forward to the street, and then turn right to approach the intersection.
- B. Start from the street side, fly upward to the roof of the building, and then move horizontally to the current position above the largest intersection
- C. Start from the park, fly straight to the building, and then arrive at the current location after circling the building
- D. Start from the scooter lane in the park, turn left to face the street outside the park, rise to the height of the top of the high-rise building across the street, and move forward to reach the intersection at the maximum upper current position
- E. Start above a building, descend to street level, then fly to a parking lot, and finally reach the current location.

Ground-Truth: B. Start from the street side, fly upward to the roof of the building, and then move horizontally to the current position above the largest intersection

ACE-Brain Output: B. Start from the street side, fly upward to the roof of the building, and then move horizontally to the current position above the largest intersection

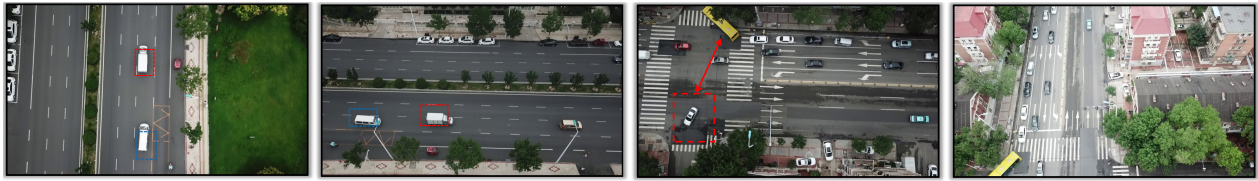
Question: At the **initial position**, you are asked to **navigate to the largest intersection nearby**. At your current location, if the maximum intersection point is not within the field of view, what is the most relevant object in the field of view and where is this object?

- Options:** A. There is a small pond at the bottom of my field of view. B. There is a row of cars parked along the street at the bottom of my view. C. The main road is in the lower part of my view. D. The biggest crossroads is in my sight. E. There is a tall building behind my view.

Ground-Truth: D. The biggest crossroads is in my sight.

ACE-Brain Output: D. The biggest crossroads is in my sight.

Figure 27 Example 1 and 2 of UrbanVideo Benchmark.



Question: Where is the white van located relative to the white truck in this scene?

Options:

- A. The white van is in the same lane as the white truck but ahead of it
- B. The white van is in a different lane and further to the left than the white truck
- C. The white van is directly behind the white truck in the same lane
- D. The white van is on the opposite side of the road from the white truck

Ground-Truth: A. The white van is in the same lane as the white truck but ahead of it

ACE-Brain Output: A. The white van is in the same lane as the white truck but ahead of it

Question: Which vehicle is positioned directly opposite the yellow bus across the intersection?

Options:

- A. The red car near the left edge of the image
- B. The white car approaching the intersection from the bottom
- C. The black car in the middle lane
- D. The teal car on the far right

Ground-Truth: B. The white car approaching the intersection from the bottom

ACE-Brain Output: B. The white car approaching the intersection from the bottom

Figure 28 Example 1 and 2 of AirCopBench.



Question: How do the vehicles at the intersection interact with the pedestrian crossing?

Options:

- A. There are no people on the zebra crossing.
- B. Vehicles are moving through the intersection without stopping
- C. Vehicles are parked along the side, not interacting with the crossing
- D. Vehicles are turning in a way that avoids the pedestrian crossing

Ground-Truth: A. There are no people on the zebra crossing

ACE-Brain Output: A. There are no people on the zebra crossing

Question: Where is the red car located relative to the white van in the same lane?

Options:

- A. The red car is directly behind the white van
- B. The red car is ahead of the white van in the opposite direction
- C. The red car is in a parallel lane to the white van
- D. The red car is parked on the side of the road near the white van

Ground-Truth: C. The red car is in a parallel lane to the white van

ACE-Brain Output: C. The red car is in a parallel lane to the white van

Figure 29 Example 3 and 4 of AirCopBench.



Question: Monica said she bought a new **brown car**. Is there a possibility of Monica's new car in the picture? Only answer yes or no.

Ground-Truth: yes

ACE-Brain Output: yes

Question: How many of the **vehicles** in the **red and blue boxes** need to go to the gas station regularly?

Options: A. 2 B. 1 C. 5 D. 4

Ground-Truth: A. 2

ACE-Brain Output: A. 2

Question: The equation of the ground plane in the **camera coordinate system** is: $-\cos(45)*y - \sin(45)*z + 30 = 0$. What are the **coordinates of the center point of the vehicle in the red box** in the camera coordinate system? (Unit: meter).

Options:

A. [24, -6, 50] B. [24, 8, 50]

C. [-22, 8, 50] D. [-23, -7, 49]

Ground-Truth: D. [-23, -7, 49]

ACE-Brain Output: D. [-23, -7, 49]

Question: The equation of the ground plane in the **camera coordinate system** is: $-\cos(45)*y - \sin(45)*z + 30 = 0$.

What are the **coordinates of the center point of the vehicle in the red box** in the camera coordinate system? (Unit: meter).

Ground-Truth: [0, 9, 32]

ACE-Brain Output:

[0.9, 3.54, 30.28]

Figure 30 Example 1-4 of AVI-Math.



Question: What's the **above ground level** of the drone when taking this photo? (Unit: meter)

Ground-Truth: 30

ACE-Brain Output: 30

Question: What are the **coordinates** of the projection point of the point 1 meter above the ground plane at the **center of the vehicle** in the pixel coordinate system?

Ground-Truth: [1148, 1666]

ACE-Brain Output:

[1184, 1428]

Question: Assuming the flight **speed** of the drone is **10 meters per second**, **how long** does it take for the drone to reach the **closest vehicle**? (Unit: second)

Ground-Truth: 6.4

ACE-Brain Output: 5.7

Figure 31 Example 5-7 of AVI-Math.



Question: What just happened?

Ground-Truth: Place the orange inside the white bowl.

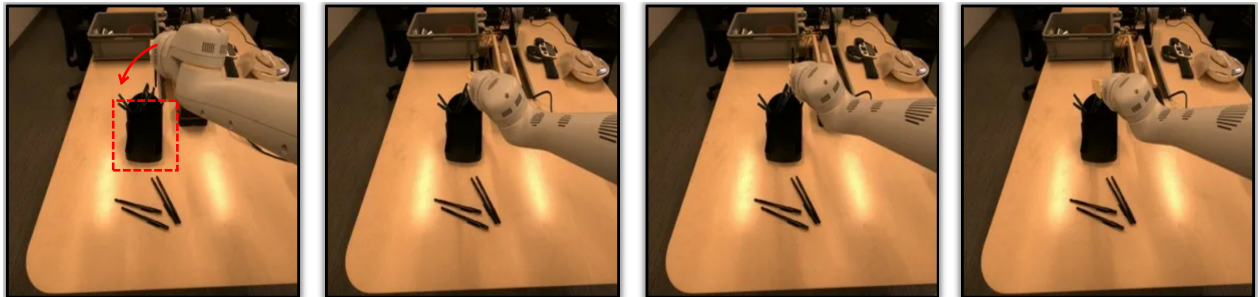
ACE-Brain Output: Put the orange into bowl.

Figure 32 Example 1 of RoboVQA Benchmark.



Question: What action is possible right now?
Ground-Truth: Place the chair away from the table.
ACE-Brain Output: Adjust the chair.

Figure 33 Example 2 of RoboVQA Benchmark.



Question: what just happened?
Ground-Truth: Drop pen into stand.
ACE-Brain Output: Place the pen into the stand.

Figure 34 Example 2 of RoboVQA Benchmark.



Question: Which room should I go to see the car?
Ground-Truth: The bedroom
ACE-Brain Output: Bedroom

Figure 35 Example 1 of OpenEQA Benchmark.



Question: Where might cotton swabs be store in this bathroom?

Ground-Truth: In the medicine cabinet above the sink.

ACE-Brain Output: In the sink cabinet.

Figure 36 Example 2 of OpenEQA Benchmark.



Question: Considering the progress shown in the video and my current observation in the last frame, what action should I take next in order to prepare bread?

Options: A. turn off sink tap B. pick plates C. adjust plates D. rotate frying pan

Ground-Truth: A. turn off sink tap

ACE-Brain Output: A. turn off sink tap

Figure 37 Example 1 of EgoPlan-Bench2 Benchmark.



Question: Considering the progress shown in the video and my current observation in the last frame, what action should I take next in order to row the boat?

Options: A. stretch legs B. ride boat C. tie shoe laces D. pick water bottle

Ground-Truth: D. pick water bottle

ACE-Brain Output: D. pick water bottle

Figure 38 Example 2 of EgoPlan-Bench2 Benchmark.